INSTITUT NATIONAL DES SCIENCES APPLIQUÉES DE LYON
École doctorale Électronique, Électrotechnique, Automatique
DEA Images et Systèmes

Modelling the response of X-ray detectors and removing artefacts in 3D tomography

Modélisation de la réponse de détecteurs de rayons X et correction d'artefacts en tomographie 3D

Franck Vidal

2002-2003

Supervisors: Dr J-M Létang & Dr G Peix
Laboratoire de Contrôle Non Destructif par Rayonnements Ionisants

INSTITUT NATIONAL DES SCIENCES APPLIQUÉES DE LYON
École doctorale Électronique, Électrotechnique, Automatique
DEA Images et Systèmes

Modelling the response of X-ray detectors and removing artefacts in 3D tomography

Modélisation de la réponse de détecteurs de rayons X et correction d'artefacts en tomographie 3D

Franck Vidal

2002-2003

Supervisors: Dr J-M Létang & Dr G Peix
Laboratoire de Contrôle Non Destructif par Rayonnements Ionisants

Acknowledgments

I would like to thank Professor Daniel Babot, head of CNDRI[1] Laboratory, for accepting me in his team. I would like to thank Dr Gilles Peix and Dr Jean-Michel Létang for proposing me this project in the field of "imaging and system" and for supporting its development.

I am also grateful to Dr Peter Clœtens from European Synchrotron Radiation Facility (ESRF) for his assistance in my research, for the use of ID19 beamline and the use of his phase contrast simulation program. I would like also to thank Professor Jean-Yves Buffière and Dr Eric Maire of GEMPPM [2] for supplying me with basic data and various information at the beginning of the work.

Generally speaking, I would like to thank all the CNDRI Laboratory team for its expertise and its well-working ambience.

[1]Contrôle Non Destructif par Rayonnements Ionisants, Non-Destructive Testing using Ionizing Radiations

[2]Groupe d'Étude de Métallurgie Physique et de Physique des Matériaux, Physical metallurgy and materials science group

Abstract

This work presents a method for modelling the response of X-ray detectors applied to remove artefacts in tomography.

On some reconstructed volumes by tomography using synchrotron radiations at ESRF, dark line artefacts (under-estimation of linear attenuation coefficients) appear when high density material are aligned.

The causes of these artefacts have been determined using experimental and simulation methods; then simulated artefacts were removed.

Finally two different causes are highlighted in this study. One of them is the impulse response of the used detector, the Frelon camera of ID19 beamline. An iterative fixed point algorithm has been used successfully to remove simulated artefacts on tomographic slices.

Keywords: tomography; X-ray; detectors response modelling; artefacts; simulation; deconvolution.

Résumé

Ce travail présente une méthode pour modéliser la réponse de détecteurs de rayons-X appliquée à la correction d'artefacts en tomographie.

Quand des matériaux de masse volumique élevée sont alignés, des lignes foncées (sous-estimation des coefficients linéaires d'atténuation) apparaissent sur des volumes reconstruits par tomographie par rayonnement synchrotron.

Les causes de ces artefacts ont été déterminées en utilisant des méthodes expérimentales et par simulations. Puis, les artefacts simulés ont été supprimés.

En définitive, cette étude a mis en évidence deux différentes causes. L'une d'elle est la réponse impulsionnelle du détecteur utilisé, la caméra Frelon de la ligne ID19. Un algorithme de point fixe a permis de supprimer efficacement les artefacts simulés sur des coupes tomographiques.

Mots-clés : tomographie ; rayons-X ; modélisation de la réponse de détecteurs ; artefacts ; simulation ; déconvolution.

Contents

Introduction

This project was proposed and supported by Dr Jean-Michel Létang and Dr Gilles Peix of CNDRI Laboratory. It comes from the collaboration between different laboratories of INSA-Lyon[3] and ESRF in Grenoble. The starting point of this research project is the disclosure of strong artefacts in specific micro-tomographic volumes acquired at ESRF on ID19 beamline by Professor Jean-Yves Buffière and Dr Eric Maire of GEMPPM. In fact, some dark lines appear when high density objects are aligned.

The subject of this study is twofold:

1. determining theoretically the origin of these artefacts using both simulation tools and real experiments,

2. proposing a method to remove them.

The whole work has been done in collaboration with Dr Peter Clœtens, member of the ID19 beamline staff.

The basics of X-ray imaging are first recalled in chapter 1. Then, an exhaustive study of possible artefacts origins is carried out in chapter 2. Having highlighted different artefact causes responsible of those dark-line artefacts, an iterative fixed point method is proposed in chapter 3 to remove them.

[3]Institut National des Sciences Appliquées de Lyon, Scientific and Technical University

Chapter 1

X-rays imaging

The German Wilhelm Conrad Röntgen discovered X-rays in 1885. They are an electromagnetic radiation (like visible radiation), generally emitted when matter is bombarded with fast electrons (X-ray tubes). X-ray beam is composed by photons. Their wavelengths are very small (typically from 10^{-10} to 10^{-14} metres). After revealing bones, Röntgen got the Nobel price in 1901 for the discovery of X-rays. Since then, X-rays imaging has been used extensively in medicine, and later on, in non-destructive testing in material science as diagnostic aid.

There are plenty of techniques to get X-rays (X-ray tube, linear accelerator, synchrotron, etc.). Nowadays, in non-destructive testing, X-ray tubes are still the main used device to produce X-rays. The first accelerators (cyclotrons) were built by particle physicists in the 1930s. Few years after, in 1947 in the USA, at General Electric, synchrotron radiation was seen for the first time [Ble93, Wil96]. Firstly, it was considered as nuisance because particles lose energy; now, synchrotron radiation sources are compared to "super-microscopes". They reveal information in numerous fields of research (*e.g.* in material science).

The European Synchrotron Radiation Facility, located in Grenoble, is a joint equipment shared by 17 European nations. The storage ring is 844 metres in circumference. Within the ring, electrons (6 GeV in energy) cover the circle in 32 straight lines and 32 turnings. At each turning (bending market) and each straight line (insertion device: wiggler or undulator at ID19), X-photons are emitted (Fig. 1.1). Photon energy is quite low (from few keV up to 100 keV), but the flux is higher (10^6 to 10^8 times more) than in the case of an X-ray tube.

1.1 Physical properties

X-photons cross matter. During their path into a sample, they can interact with matter [AR68]. Fig. 1.2 illustrates interactions and image forming. For most X-rays imaging modalities, only directly transmitted photons are essential, because they project an image of the sample on the detector. The quality of images depends on interactions into samples and into the detector. Scattering participates in the image forming and degrades the image quality. There are five kinds of interaction,

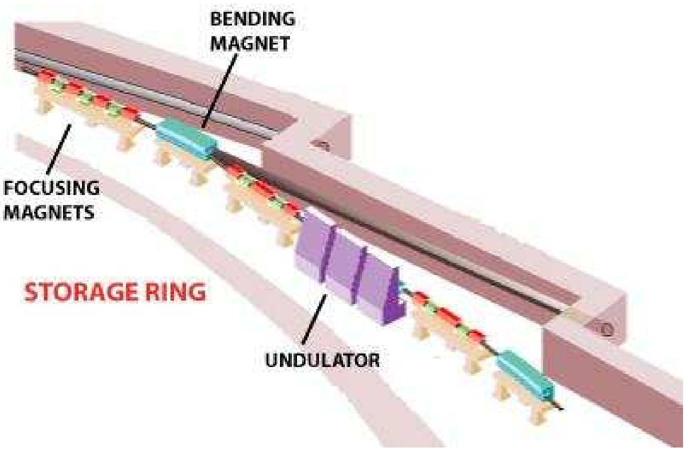

Figure 1.1: Storage ring includes straight and curved sections (This picture comes from the ESRF web site [ESR03]).

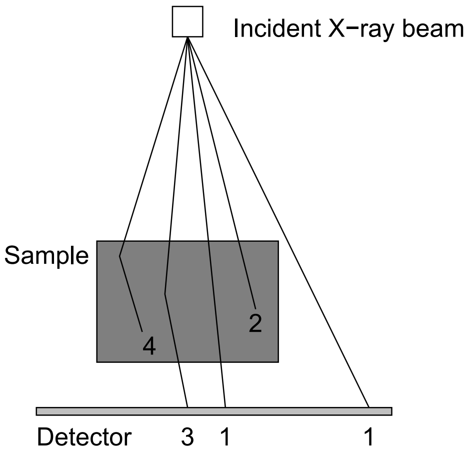

Figure 1.2: X-photons/matter interactions. 1 Directly transmitted photons (no interaction). 2 Absorbed photons. 3 Scattered photons. 4 Absorbed scattered photons.

- photoelectric effect,
  The energy of a photon is completely absorbed by an atom. Its energy is transfered to an electron of an internal layer (generally K or L). This electron is ejected from its atomic orbital with an kinetic energy E_c.

$$E_c = E_0 - E_1 \tag{1.1}$$

  with E_0 the incident photon energy and E_1 the bonding energy of the concerned layer.
  The ionization of this electron layer is followed by the emission of a X-fluorescence photon or an Auger electron (probability of Auger effect is important for low atomic number). Generally, fluorescence photon is absorbed near the interaction place because of its low energy.

- Rayleigh scattering (or coherent scattering),
  As a first approximation, photons can be considered deviated from their direction without energy loss.

- Compton effect (or incoherent scattering),
  This effect is the result of an elastic shock between an electron and an incident photon. This electron is free or weakly linked to the atom. The photon transfers a part of its energy to the electron. The photon is scattered, and the electron gets kinetic energy.

- pairs creation,
  This effect is based on the conversion of incident photon energy into mass energy. An electric field is around the nucleus of an atom (or around an electron). This field can transform the incident photon into matter. This matter corresponds to a pair of electron-positron. It only appears when incident energy is superior to 1.02 MeV (minimum energy corresponding to the mass creation).

- nuclear reaction,
  A high energy photon (from 6 to 15 MeV) can be absorbed by a nucleus. The nucleus becomes instable. It disintegrates and emits a proton or a neutron.

1.2 Beer-Lambert law (or attenuation law)

Along a given X-ray path, let N be the number of photons at abscissa x. The number of photons dN, which will interact along an infinitesimal distance dx, is given by:

$$\mathrm{d}N = -\mu N \mathrm{d}x \tag{1.2}$$

Coefficient μ, which can be seen as a probability of interaction by length unit, is also called linear attenuation coefficient. It is usually expressed in cm^{-1}. It depends on:

1. E, the energy of incident photons,
2. ρ, the material density of the sample,
3. Z, the material atomic number of the sample.

Eq. 1.2 can be integrated over the spatial and energy domain. Let N_0 be the number of incident photons. The total number of transmitted photons, N_1, becomes:

$$\int N_1(E)\mathrm{d}E = \int N_0(E) \times \exp\left(-\int \mu(\rho(x), Z(x), E)\mathrm{d}x\right)\mathrm{d}E \tag{1.3}$$

This integrated form is the Beer-Lambert law. Simplified forms can be used, for example when the incident X-ray beam is monochromatic:

$$N_1 = N_0 \times \exp\left(-\int \mu(\rho(x), Z(x))\mathrm{d}x\right) \tag{1.4}$$

Furthermore, for homogeneous materials, we get

$$N_1 = N_0 \times e^{-\mu x} \tag{1.5}$$

Note that generally, μ is not directly used. The mass attenuation coefficient $\frac{\mu}{\rho}$ (in $cm^2.g^{-1}$) is preferred. This coefficient does not depends on the density and the state of the material. At a particular energy, $\frac{\mu}{\rho}$ is constant for a given chemical composition (*e.g.* $(\frac{\mu}{\rho})_{ice} = (\frac{\mu}{\rho})_{water} = (\frac{\mu}{\rho})_{vapour}$).

1.3 Tomography

Tomography is a non-destructive method. It is a multi-angular analysis followed by a mathematical reconstruction (Fig. 1.3). Tomographic acquisition consists in acquiring many projections. Between each projection, depending on the context, either the sample (in NDT) or the couple detector/source (in medical scanners) is rotated and/or translated.

The first classical tomographic device was introduced in 1921. In 1972, Hounsfield tested successfully the first clinical Computerized Axial Tomography (CAT[1]) [Hou73, Pey03].

The reconstruction process is a mathematical routine that consists in back-projecting into the object space a physical variable whose measures are integral quantities along strait lines. We saw in the previous section from the Beer-Lambert law, that an X-ray projection delivers at each pixel an integral measure of the attenuation coefficient. Therefore after reconstruction, a tomographic slice ideally corresponds to a linear attenuation coefficient μ map. However, as we will see in chapter 2, there are many artefact causes, and quantitative imaging via tomography is highly sensitive. There are two kinds of reconstruction algorithm:

- analytic methods [DG02, KS88],
- algebraic methods [BP02].

[1] generally reduced as Computerized Tomography (CT)

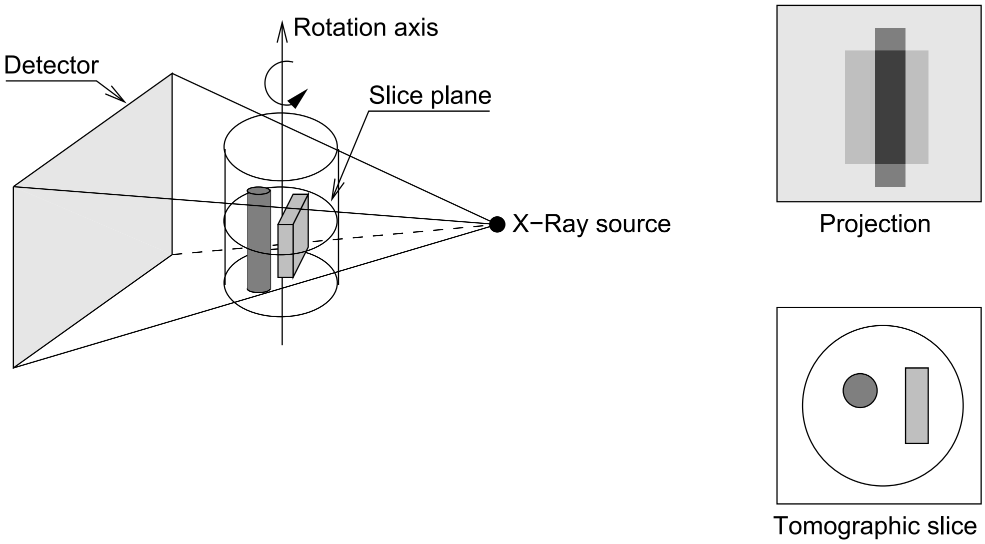

Figure 1.3: X-ray tomography.

1.3.1 Analytic reconstruction methods

Analytic methods are based on a continuous modelling. Reconstruction consists in the inversion of measurement equations. The most frequently used is the filtered back-projection algorithm (FBP).

Following Fig. 1.4, the expression of a projection is Eq. 1.6.

$$P_\theta(u) = \int\int f(x,y)\delta(u - x\cos\theta - y\sin\theta)\mathrm{d}x\mathrm{d}y \tag{1.6}$$

There is a relationship between the expression of a projection (Eq. 1.6) and the Radon transform (Eq. 1.7 & Eq. 1.8)

$$R_f(t,\theta) = P_\theta(t) \tag{1.7}$$

$$R_f(t,\theta) = \int\int f(x,y)\delta(t - x\cos\theta - y\sin\theta)\mathrm{d}x\mathrm{d}y \tag{1.8}$$

Fig. 1.5 illustrates the reconstruction process. The sinogram, which is the observed measure, is built from the set of X-ray projections at successive angles. Tomographic reconstruction consists in estimating the original object from this sinogram. Analytic methods inverse the Radon transform using the Fourier slice theorem: the 1D Fourier transform of a projection is equal to a slice of the 2D Fourier transform of the original image. The complete 2D Fourier transform of the image is reconstructed from these 1D Fourier transforms. Then, the image is obtained by inverting its Fourier transform.

1.3.2 Discrete reconstruction methods

These reconstruction techniques are based on iterative correction algorithms. For example in the Algebraic Reconstruction Technique (ART), one of the most commonly used algorithm,

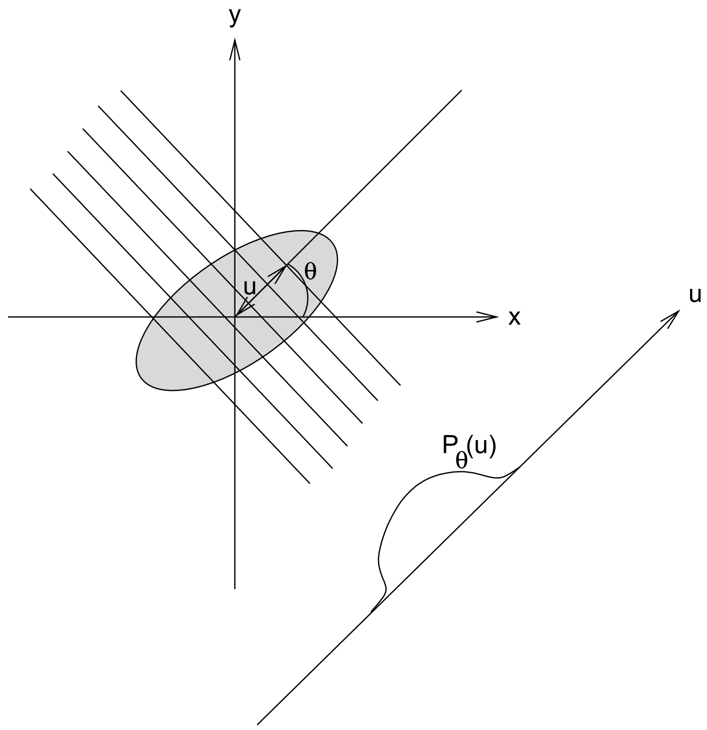

Figure 1.4: Projection expression.

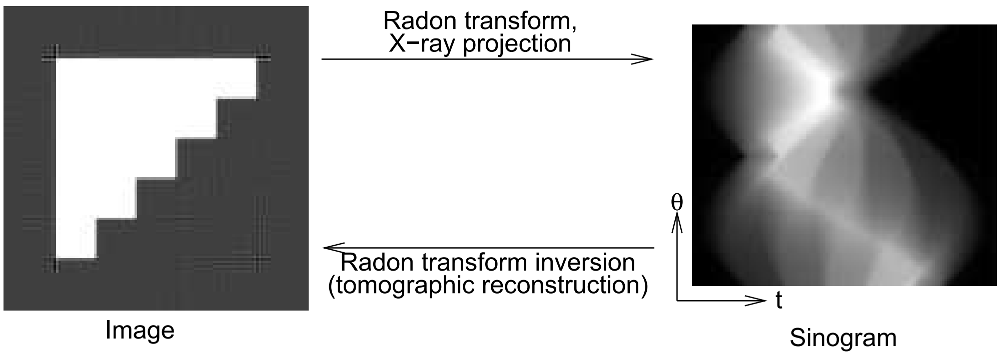

Figure 1.5: Inverse problem: reconstruction of an unknown image from a known sinogram.

an iteration consists in updating the reconstructed volume for each measurement pixel location, *i.e.* ray by ray. Besides ART, there are many other iterative techniques, namely Simultaneous ART (SART), Multiple ART (MART), Simultaneous Iterative Reconstruction Technique (SIRT), etc.

For more details about tomographic reconstruction, it is recommended to have a look at specific literature [BP02, Cen98, DG02, KS88].

1.4 Simulation

The whole X-ray imaging chain, from the source to the detector, can be simulated by computing. There are plenty of simulation tools. Such programs are very useful. For example, they allow scientists to understand how photons cross matter. They also allow engineers to simulate experiment, and optimize experiment parameters [BCL02, LFP03]. They also permit to conceive new imaging system [Lec02].

There are two different kinds of X-ray simulation algorithms:

- probabilistic method, based on Monte Carlo trials,
- determinist or analytic method, based on ray-tracing.

1.4.1 Monte Carlo method

Simulation by Monte Carlo [BCL02, SFAS01] consists in the individual tracking of each particle (*e.g.* photon in the case of X-ray simulation). Such algorithms are able to follow each photon during its different interactions with matter. At each step of the simulation, several events are possible for each photon. Events are chosen randomly. The events probability respects physical law probabilities. Naturally, the quality of a such algorithm depends on the quality of the random numbers generator.

For carrying out our probabilistic simulations, GEANT4[2] [Ama00] developed by the CERN[3] has been used. It is a library for simulating the passage of particles (not only X-ray photons) through matter. At CNDRI Lab., GEANT4 has been historically chosen because:

- the same physical models, as VXI (presented in subsection 1.4.2), are used. The same cross sections database [CHK97] are used in both simulation toolkits.
- It is a library written in C++ and it uses object-oriented programming (OOP) concept.

[2]The acronym GEANT comes from GEometry ANd Tracking
[3]Conseil Européen de la Recherche Nucléaire

1.4.2 Ray-tracing algorithm

Ray-tracing is a determinist algorithm. Originally, it has been designed to image synthesis in the visible domain. In the 3D space, a straight line from the observer (often called camera) to a pixel of the projection plane is called a ray. For each pixel, intersections of a ray with objects must be calculated. There is an intersection, when a ray comes into an object, or when a ray goes out. But only the closest intersection to the observer is useful, others are not visible by the observer [FvFH97]. It is illustrated by Fig. 1.6. As there are two objects in this figure, there are

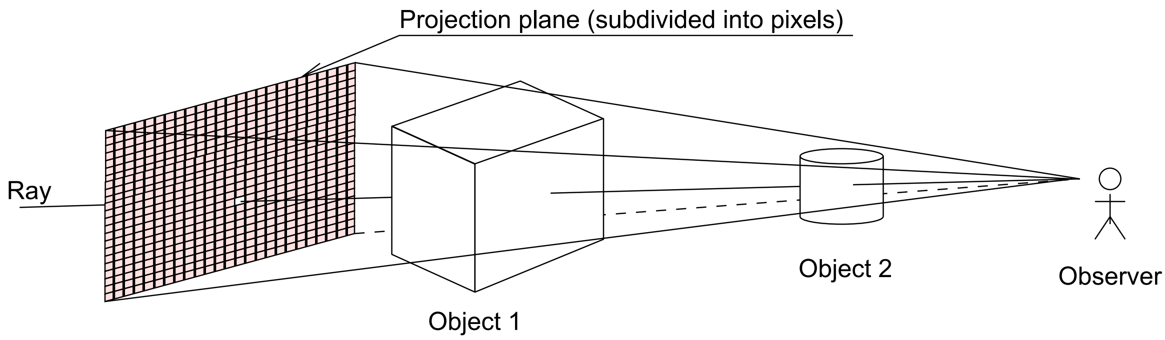

Figure 1.6: Image synthesis by ray-tracing in the visible domain. A ray is drawn from the observer through each pixel.

four intersections of the ray with objects. The pixel color has to be computed considering the nearest intersection to the observer.

Ray-tracing principle has been adapted to X-ray simulation. In this case, all intersections have to be considered. It allows to compute radiation attenuation considering the thickness crossed by a ray into an object characterized by its material.

Virtual X-ray Imaging (VXI) is an X-ray simulation toolkit, written in C++. It has been developed at CNDRI laboratory [DFK$^+$00, DFKB00, Fre03]. Input data is composed by 3D objects described by triangles networks (known as polygon meshes). This standard representation allows to use Computer-Aided Design (CAD). It is useful to deal with complex three-dimensional (3D) geometry (Fig. 1.7). Another interest of the use of polygon meshes is to make the render process faster. Indeed, number of algorithms have been developed for such geometry representation. For example, Z-buffer algorithm was introduced in 1974 by Catmull [Wat00]. The original purpose of this algorithm is to remove hidden faces. Nowadays, it is used for real-time rendering of polygons [WND$^+$97]. It has been adapted to ray-tracing. Then, in VXI, it has been adapted to X-ray simulation.

1.4.3 Comparison

These two kinds of algorithm are not rival, they are complementary.

- The first is slow. Several days can be needed to get image with an acceptable noise level

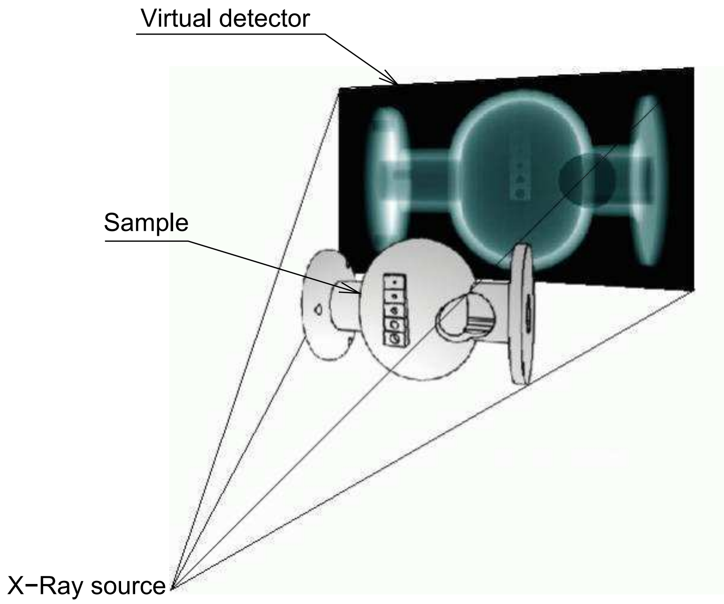

Figure 1.7: Radiographic simulation with VXI. A point source, a matrix detector and a CAD model with triangular meshes.

(*e.g.* 1%). But, following physical law, it takes each kind of photon/matter interactions into account (scattering, fluorescence, electron processes, etc.).

- The second is fast. It does not produce noise. It can be added after, to simulate realistic images. Sinogram (900 projections of 4096 ×1 pixels) can be simulated in few minutes (less than 5 minutes) using current computer (Pentium III, 1 GHz). But it is only really suited to directly transmitted photons.

In the following chapter, we will see that both methods were used in this study to determine the origin of artefacts. Indeed, depending on the goal of the simulation experiment, VXI is useful when only directly transmitted photons have to be considered. But GEANT4 is definitely required to estimate the role played by each kind of interactions.

Chapter 2

Potential artefacts sources

2.1 Introduction

We shown in section 1.3 that, given an ideal detector and a monochromatic X-ray spectrum, the volume reconstructed by tomography is a map of linear attenuation coefficients for that particular energy. However in practice, many artefacts occur in reconstructed volumes. As an example, Fig. 2.1 shows a typical reconstructed slice of a aluminium composite acquired at ESRF.

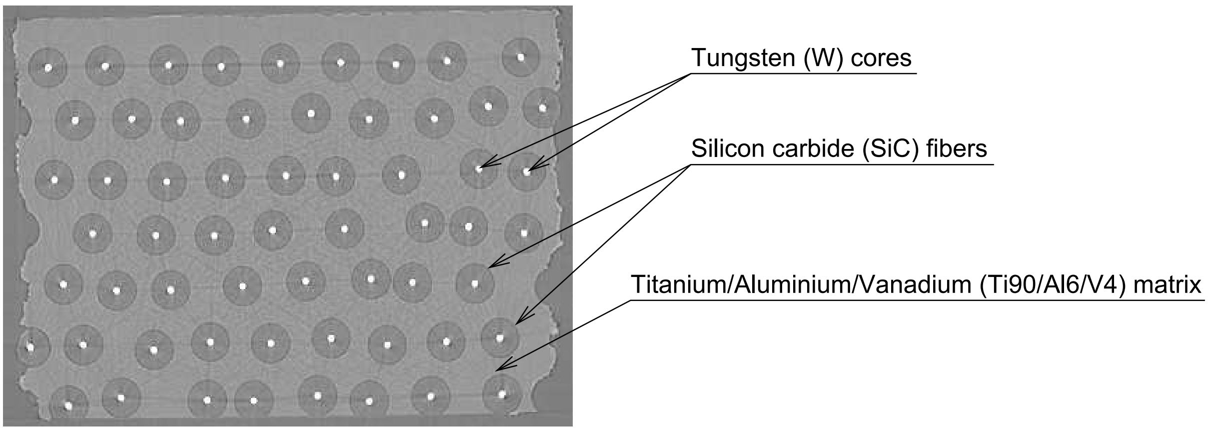

Figure 2.1: Slice reconstructed by tomography, containing artefacts. Experiment carried out at the ESRF on ID19 beamline. Large distance between source and detector, 145 m (parallel photons beam). Distance between detector and inspected object, 80 mm. Detector, a CCD camera with a 1024 × 615 pixels resolution. 1.9 µm pixel size. Synchrotron radiation, 33 keV in energy. 900 projections, angular span 180°.

Two kinds of artefacts are clearly visible in Fig. 2.2, an enlarged region of interest (ROI) of Fig. 2.1. Black and white rings are well known phase contrast artefacts. Physicians are not annoyed by these artefacts. But the dark lines with bright borders, located along alignments of high density tungsten cores, are more disturbing. Indeed tungsten cores, silicon carbide fibers and titanium matrix are homogeneous materials. As these lines are darker, linear attenuation coefficients are under-estimated on artefacts area. Using a database, it is possible to obtain the-

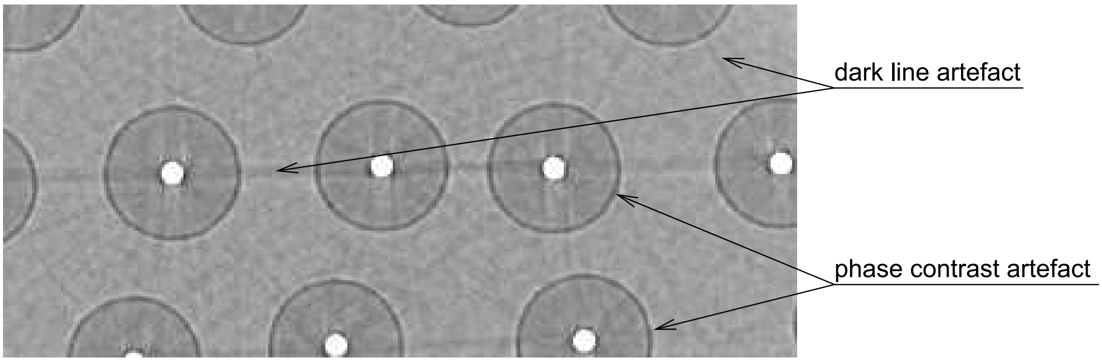

Figure 2.2: Extract of Fig. 2.1.

oretical attenuation coefficient in any element, compound or mixture, at energies from 1 keV to 100 GeV [BH87, BHS$^+$99]. Comparing attenuation coefficients given in the center of reconstructed slice using real data to these theoretical coefficients, it has been detected that the computed coefficients are false (the center of the slice is used because this area is reconstructed using more data than the periphery of the slice).

- Silicon carbide total mass attenuation at 33 keV is 0.855 $cm^2.g^{-1}$. Its density is 3.2 $g.cm^{-3}$ [Cor03a]. The theoretical linear attenuation coefficient is obtained as follows: $0.855 \times 3.2 = 2.736$ cm^{-1}. The experiment gives values varying between 0 and 10 cm^{-1}.

- Total mass attenuation at 33 keV of the aluminium composite Ti90/Al6/V4 is 2.97 $cm^2.g^{-1}$. Its density is 4.42 $g.cm^{-3}$ [Cor03b]. The theoretical linear attenuation coefficient is obtained as follows: $2.97 \times 4.42 = 13.1274$ cm^{-1}. The experiment gives values varying between 10 and 18 cm^{-1}.

- Tungsten total mass attenuation at 33 keV is 17.7 $cm^2.g^{-1}$. Its density is 19.3 $g.cm^{-3}$. The theoretical linear attenuation coefficient is obtained as follows: $17.7 \times 19.3 = 341.61$ cm^{-1}. The experiment gives values varying between 165 and 185 cm^{-1}.

This kind of artefacts is a new problem for physicians studying materials, since it has not been detected previously in quite similar aluminium composites [MB00]. Fig. 2.3 is the result of a tomographic reconstruction where the cores are in carbon, which does not absorb X-rays much, compared to tungsten. Phase contrast is still visible, but there are no dark lines any longer.

In this study, we decided to focus the application context on this aluminium composite with tungsten fiber cores. The goal is the complete understanding and evaluation of all possible artefact causes, using both real experiments and simulation tools. First in section 2.2 we evaluate the importance of each photon/matter interactions and their respective degradation on the X-ray image. Section 2.3 reviews sampling artefacts. The role of harmonic components present in the ESRF source is studied in section 2.4. Degradations due to the detector's response are estimated in section 2.5. Finally phase contrast artefacts are evaluated in section 2.6.

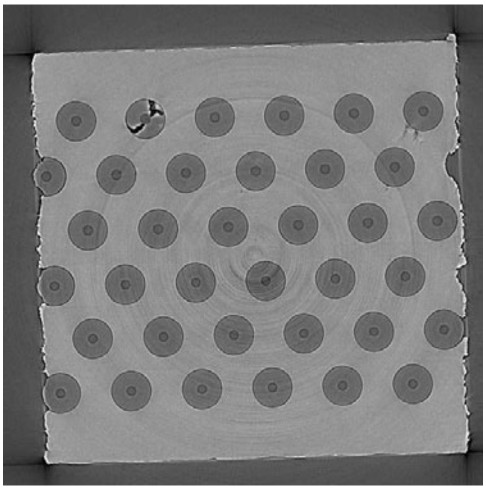

Figure 2.3: Slice of volume of a carbon fiber reconstructed by tomography. Experiment carried out at the ESRF on beam line ID19, with a distance between the source and the detector of 140 m. Distance between detector and inspected object, 60 mm. Pixels size in reconstructed image, 2.8 µm. Electron beam energy, 30 keV. 1200 projections performed around the object, on 180°.

2.2 Interactions

In this section, we evaluate the relative importance of direct radiations with respect to other radiations (scattering, fluorescence, etc.) that can be expected in the aluminium composite with tungsten core fibers.

2.2.1 3D scene to simulate

We have listed in section 1.1 the different kinds of interaction that can take place between photons and matter. Basically, three main types are likely to degrade X-ray images:

- Rayleigh scattering,
- Compton scattering,
- Fluorescence photons emission.

It was seen, in subsection 1.4.1, that Monte Carlo method algorithms are able to follow each photon during its different interactions with matter. It allows to determine whether a particular kind of interactions is enough important to generate such artefacts.

Fig. 2.4 illustrates the 3D scene, which has been used for the simulation. The 3D scene is composed of a monochromatic parallel X-ray source at 33 keV, an aluminium composite simulation phantom and a detector. This simulation setup is similar to the one used in the real experiment.

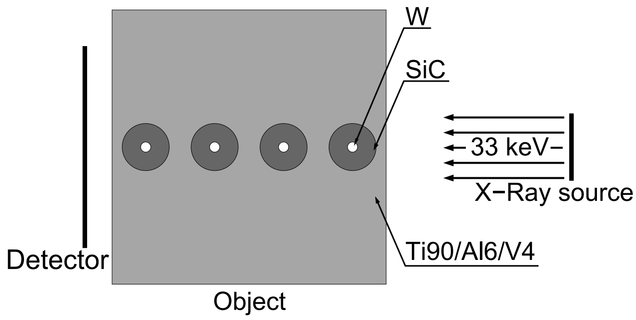

Figure 2.4: Scene simulated with GEANT4. *Tungsten cores diameter, 30 µm. Silicon carbide fibers diameter, 140 µm. Matrix size,* 815×815 *µm. Distance between detector and object, 80 mm. Parallel monochromatic X-rays, 33 keV in energy.*

2.2.2 Using small size with GEANT4

We first entered in GEANT4 the true composite geometry (see Fig. 2.4), *i.e.* silicon carbide fibers of 140 µm diameter with tungsten cores of 30 µm diameter. However with objects of very small sizes, typically the fiber cores, the GEANT4 simulation always crashed. To solve this problem, we had to transpose the simulation setup.

Let us first show that the X-ray simulation experiment remains the same when all geometric dimensions, including the detector, are scaled inversely to the material densities. We know from the Beer-Lambert law in section 1.2 that, for a given chemical composition (mass attenuation coefficient μ/ρ is fixed), the photon transportation's probability law is determined by the product of the local density by the track length. This is valid for any photon, whether direct, scattering or fluorescent. This means that if we transpose the initial simulation setup by scaling up all geometrical dimension by a given factor (typically 1000), the transposed X-ray simulation will be the equivalent as long as material densities are scaled down by the same factor.

To validate this transposition, we designed a specific simulation setup, where Rayleigh and Compton photons are sufficiently present to show the statistical equivalence of the transposition. An iron box of $100 \times 100 \times 50$ in mm, with a cavity of $20 \times 5 \times 2.5$ in mm is placed in front of a lead filter ($300 \times 300 \times 1$ in mm) using fan-beam of 400 keV. Two different simulations have been performed, one with the true geometry, one with a transposition factor of 1000. Fig. 2.5 clearly shows that this scaling factor does not alter direct nor the scattered radiations. Both simulations are statistically identical. Images and profiles resulting from multiple scattering are presented in App. A.

2.2.3 Simulation of the aluminium composite

We showed in previous subsection that a simulation experiment can be transposed without harming the result validity by inversely scaling geometrical dimensions and material densities. To avoid GEANT4's crash with small cylinder dimensions, the aluminium composite is used with a transposition scaling factor of 1000. Fig. 2.6 presents results of the simulation performed with this setup. On these figure, we display i) directly transmitted photons ii) all photons (directly

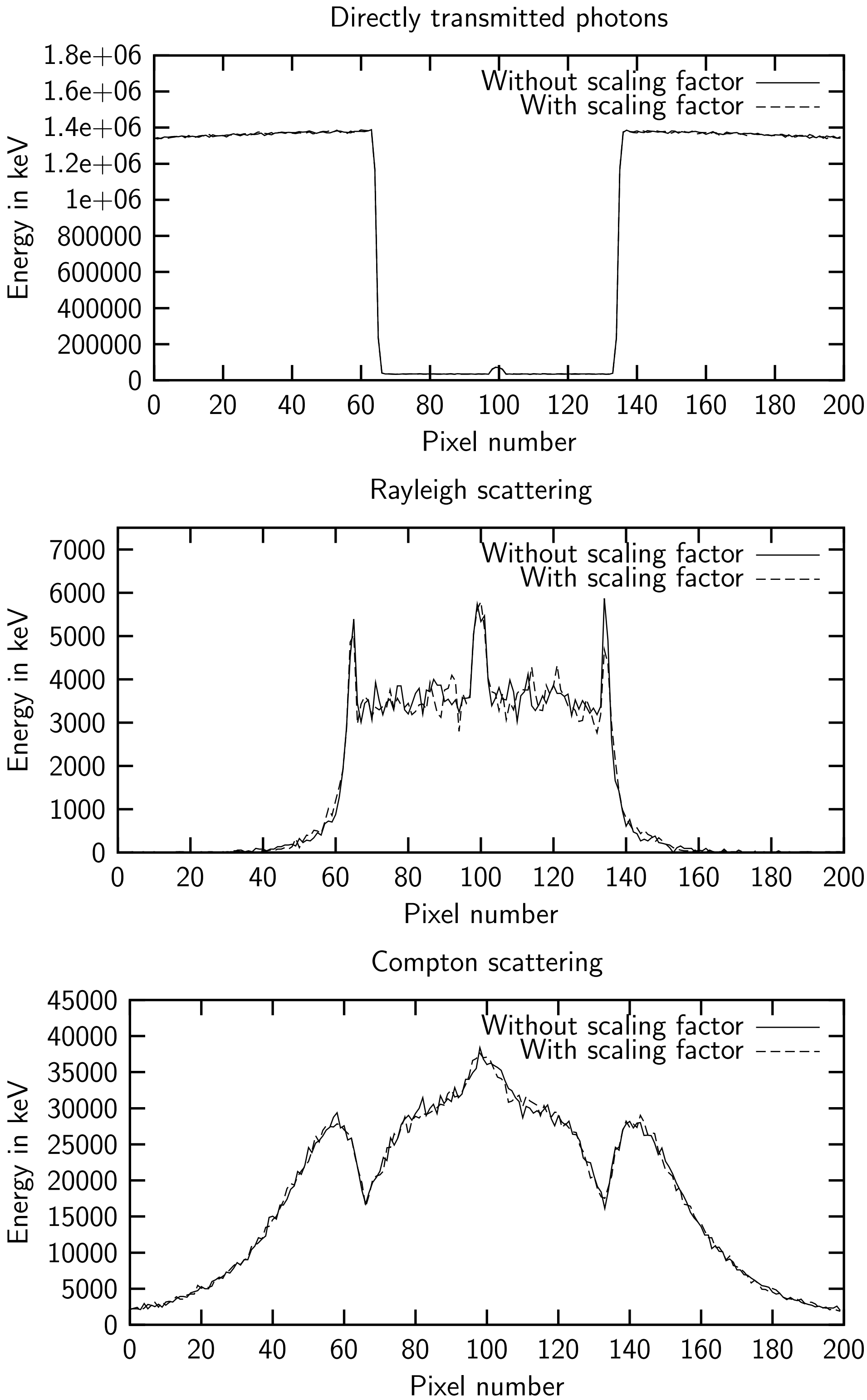

Figure 2.5: Average vertical profiles of a simulation of a filter ($300 \times 300 \times 1$ *in mm) in lead at the front of an iron box of* $100 \times 100 \times 50$ *in mm, with a little cavity of* $20 \times 5 \times 2.5$ *in mm, using fan-beam of 400 keV.*

transmitted and scattered photons).

On Fig. 2.6.a, the two curves are superposed, showing that only directly transmitted photons are important. By zooming on pixel 295 to 300 (area where there is the less directly transmitted photons), the curves are still very close (Fig. 2.6.b).

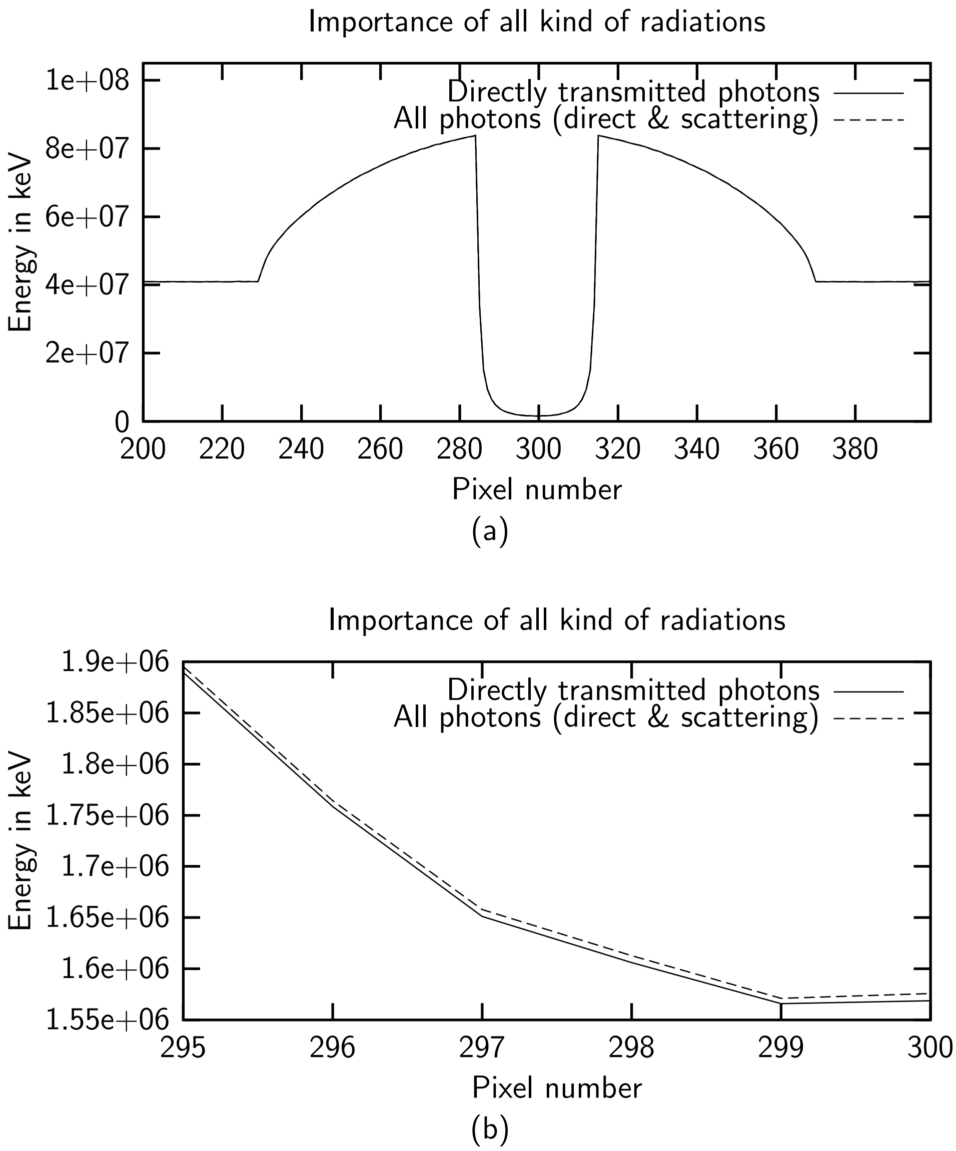

Figure 2.6: Results of the simulation corresponding to the setup presented in Fig. 2.4. Calculation time $\simeq$ 1 week.

In the setup presented in Fig. 2.4, 99.97% of the energy received by the detector is directly transmitted. Other photons received by the detector represent 0.03% of the received total energy, among which:

Radiation	Percentage in energy received
Rayleigh	93.47%
Compton	5.35%
Scattering photons (order 2)	1.15%
Scattering photons (order 3)	0.01%
Scattering photons (order N)	0.00%
Fluorescence & Bremsstrahlung photons	0.02%

More than 99 percents of the energy received by the virtual detector come from directly transmitted photons. According to these results, scattering, fluorescence and Bremsstrahlung photons are negligible, then they can be ignored. The dark line artefacts cannot be present on account of non direct photons in this aluminium composite. Moreover, to get a high resolution image from Monte Carlo algorithm, the calculation time is too long for current computers. As only directly transmitted photons are significant, ray-tracing simulation can be used for future experiments. It is a faster technique, which enables tomographic acquisition simulations in an acceptable computation time.

2.3 Aliasing

Considering the rendering time, it is not currently possible to simulate tomography using Monte Carlo algorithm with a PC. But in the previous section, it was seen that the scattering photons, fluorescence and Bremsstrahlung are not enough important. Consequently, from now, simulations can be performed using a ray-tracing algorithm.

Two methodology parameters have to be taken into account when a tomographic acquisition is simulated: the number of pixels of the detector and the number of projections. Nyquist observed that a signal must be sampled at least twice during each cycle of the highest frequency of the signal. Let us consider n, the number of pixel of the detector and p the number of projections uniformly distributed over 180°. If projection data are under-sampled or if not enough projections are recorded, then there will be insufficiency of data. Artefacts on account of insufficiency of data are usually called the aliasing distortions. According to [Pey03] and [KS88], the Nyquist theorem is satisfied when the number of projections is:

$$\frac{\pi}{2} \times n \leq p \tag{2.1}$$

In the case of parallel beam, these projections are uniformly distributed over 180°.

To verify the effect of aliasing in our case, different tomographic scans have been simulated with different number of pixels and projections. Fig. 2.7 shows the effects of under and over-samplings. The number of pixel is constant (1024), only the number of projections varies in these examples. According to Eq. 2.1, at least 1609 projections are needed for a 180° angular span if there are 1024 pixels per projection.

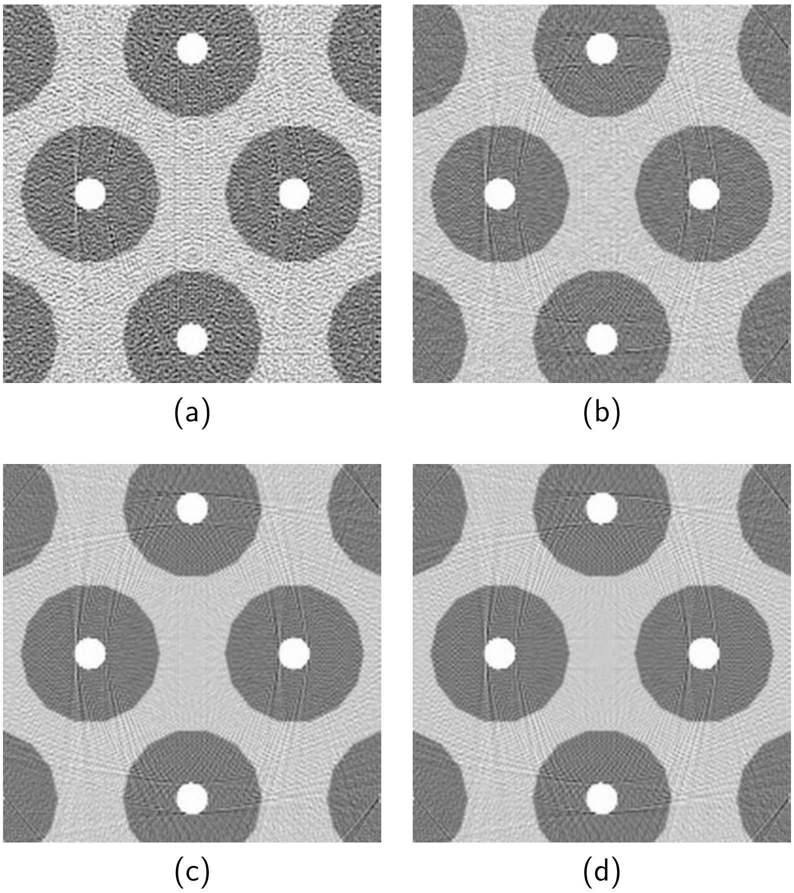

Figure 2.7: Extracts of slice of a tungsten fiber, reconstructed by tomography using a monochromatic beam, 33 keV in energy, 1024 pixels, angular span 180°. (a) 450 projections; (b) 900 projections; (c) 1800 projections; (d) 3600 projections.

Under-sampling decreases the visual quality of reconstructed slices. On the other hand, over-sampling increases a little bit the image quality. Although only 900 projections were acquired at ESRF, the few artefacts caused by aliasing are not similar to those on real slices.

2.4 Harmonic components

Simulations performed in previous sections used setups with a monochromatic source. However synchrotron radiation produces a polychromatic spectrum. To obtain a monochromatic beam at a given energy, this spectrum is filtered by a multi-layer monochromator. But in the worst case, this spectrum can be corrupted by typically a few percent of harmonic components.

A new simulation setup has been designed to evaluate the degradation due to these harmonic components. We heuristically decided to split the incident spectrum energy into three components:

- the fundamental component, 33 keV in energy, 97% of the incident beam,

- the 1st harmonic component, 66 keV in energy, 2% of incident the beam,
- the 2nd harmonic component, 99 keV in energy, 1% of incident the beam.

A reconstructed slice of this setup is shown on the left-hand side of Fig. 2.8. Such incident

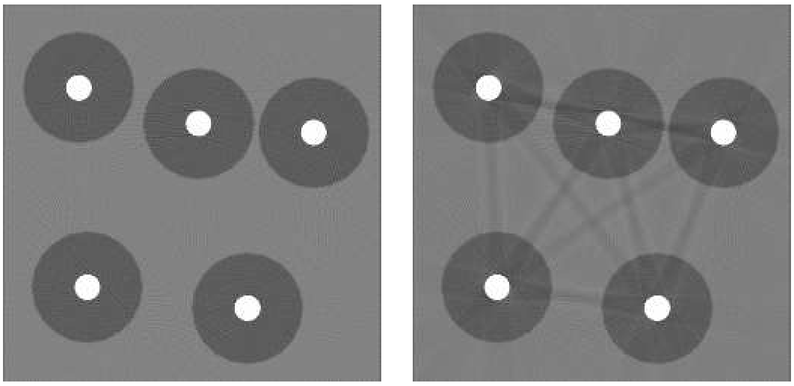

(a) (b)

Figure 2.8: Effect of harmonic components on tomographic slice simulation. Distance between detector and sample, 80 mm. Pixel size 1.9 µm. 900 projections, angular span 180°. (a) monochromatic beam, 33 keV in energy. (b) polychromatic beam (33 keV: 97% of the incident beam, 66 keV: 2% of the incident beam, 99 keV: 1% of the incident beam).

beam produces artefacts onto the reconstructed image. Dark lines with bright borders appear, when high density material are aligned. These artefacts are similar to those observed on slices reconstructed from experimental data (Fig. 2.2). In this study, the correction of harmonic components is not supposed to be done. Indeed, methods already exist in the case of tomographic acquisition using X-ray tube. They can be also used in the case of synchrotron. Moreover it is possible to use a silicium monocrystal monochromator, which will reduce harmonic components; unfortunately, it will increase the acquisition time comparing to the use of the multilayer one. Anyway, dark lines only appear when high density samples are aligned, then a such monochromator can be only used with this kind of material.

2.5 Response of the detector

Until now, to determine the origin of dark line artefacts, only simulation with perfect detector have been performed. Unfortunately, for real experiments, detectors do not have an ideal response.

In this study, experimental data has been obtained at ID19 beamline using the FRELON[1] camera. It is a 14 bit dynamic CCD detector, with a 1024 × 1024 pixel chip or a 2048 × 2048 pixel chip [CP02, ID103]. It has been developed by the 'Analog and Transient Electronic' ESRF group. The whole acquisition system is composed by:

[1]Fast REadout LOw Noise

- a shutter,
- an x-ray to visible light converter (fluorescent screen),
- an optical system,
- a CCD camera.

The shutter allows to stop the exposure of the CCD camera during its reading time. Optical system determines image pixel size. In the case of this study, only 1.9 µm is considered.

2.5.1 Introduction

Acquisition systems cannot perfectly reproduce the input data. There is always more or less noise, images are always more or less blurred. In X-ray imaging, the main causes of blur (or unsharpness) are:

1. X-ray source focus size (geometrical unsharpness) (Fig. 2.9),
2. detector impulse response (detector inherent unsharpness) (Fig. 2.10).

The detector inherent unsharpness can be due to pixel size, scattering inside the fluorescent screen and its support, optical lenses, etc.

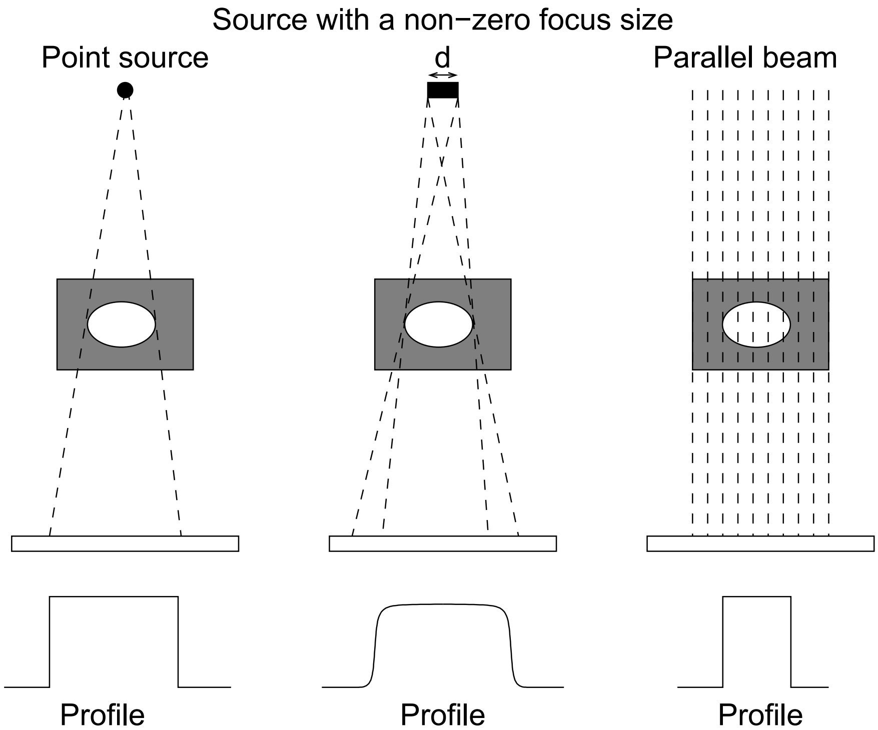

Figure 2.9: Geometrical unsharpness.

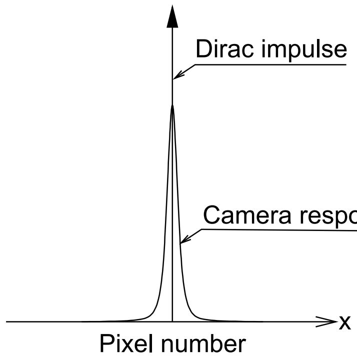

Figure 2.10: Detector inherent unsharpness.

It is possible to estimate and combine different causes of unsharpness. The result of these estimations is an unsharpness function. In the geometric domain, this function is called point spread function (PSF). It corresponds to the response of the detector to one Dirac impulse (Fig. 2.10). In the Fourier domain, it is defined as the transfer function. Its magnitude is called modulation transfer function (MTF). It is often used to characterize the spatial resolution of an imaging system [Hol96, KZR$^+$96]. MTF and PSF are closely connected with the whole acquisition system (CCD camera, converters and optics). For each optic, MTF and PSF will change. Moreover, geometrical unsharpness function is closely connected with the distance of the sample to the source, in the case of a fan-beam source with a non-zero focus size. But in the case of parallel beam, there is no geometrical unsharpness. Then the PSF is equivalent to a convolution by a low pass filter (see [GW77] to get details on convolution).

2.5.2 Suspecting the impulse response

We saw in the previous subsection that the effect of the impulse response is similar to a convolution by a low-pass filter. Here, we will theoretically demonstrate that the impulse response is influent when several samples are aligned.

Let us consider the case of a monochromatic and parallel incident beam. A sample is made of an homogeneous material characterized by its linear attenuation coefficient μ and its thickness x. N similar samples are aligned at the front of a given pixel t. The width of a pixel is equal to the width of a sample. Consider E_0, E and E_r respectively the incident energy, the energy received by an ideal detector behind N samples and the energy received by a real detector behind N samples.

1. Fig. 2.11 illustrates the energy received by an ideal detector; the PSF width is null.

   At the pixel t, the fall is $E_0 - E$.

   (a) If there is only one sample ($N = 1$) at the front of the pixel t, then we will get from the Beer-Lambert law (Eq. 1.5):

$$E = E_0 \times e^{-\mu x} \tag{2.2}$$

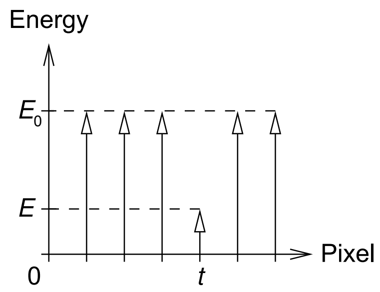

Figure 2.11: Energy received by an ideal detector.

The measure given by the detector is:

$$\ln \frac{E_0}{E} = \mu x \tag{2.3}$$

(b) In the case of several aligned samples ($N > 1$), we get:

$$E = E_0 \times e^{-\mu N x} \tag{2.4}$$

and the measure given by the detector is:

$$\ln \frac{E_0}{E} = N \mu x \tag{2.5}$$

As expected, we note that <u>using an ideal detector, measures vary linearly in N</u>.

2. Fig. 2.12 illustrates the energy received by a <u>real detector</u>; the PSF width is not null.

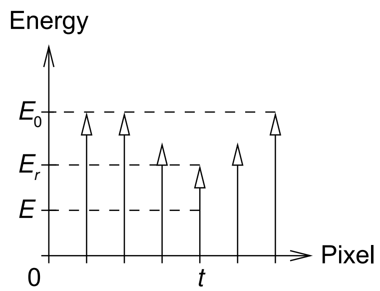

Figure 2.12: Energy received by a real detector.

At the pixel t, the fall is $k(E_0 - E)$, with $k \in [0, 1]$. The real value, E_r, is:

$$E_r = E_0 - k(E_0 - E) \tag{2.6}$$

$$E_r = E_0 - kE_0 + kE_0 \times e^{-\mu N x} \tag{2.7}$$

$$E_r = E_0\left(1 - k + ke^{-\mu N x}\right) \tag{2.8}$$

The measure given by the detector becomes:

$$\ln\frac{E_0}{E_r} = -\ln(1 - k + k \times \exp(-\mu N x)) \tag{2.9}$$

Using a real detector, measures do not vary linearly in N anymore.

Fig. 2.13 illustrates the influence of the number of aligned samples and the material. If k is equal to 1, then Eq. 2.9 is equivalent to Eq. 2.5. In this example, although k is equal to 0.9, the figure clearly shows that the impulse response only really play a role when high density material are aligned. Its role can be ignored with low density material. It can explain why the dark line artefacts do not appear with carbon cores (Fig. 2.3).

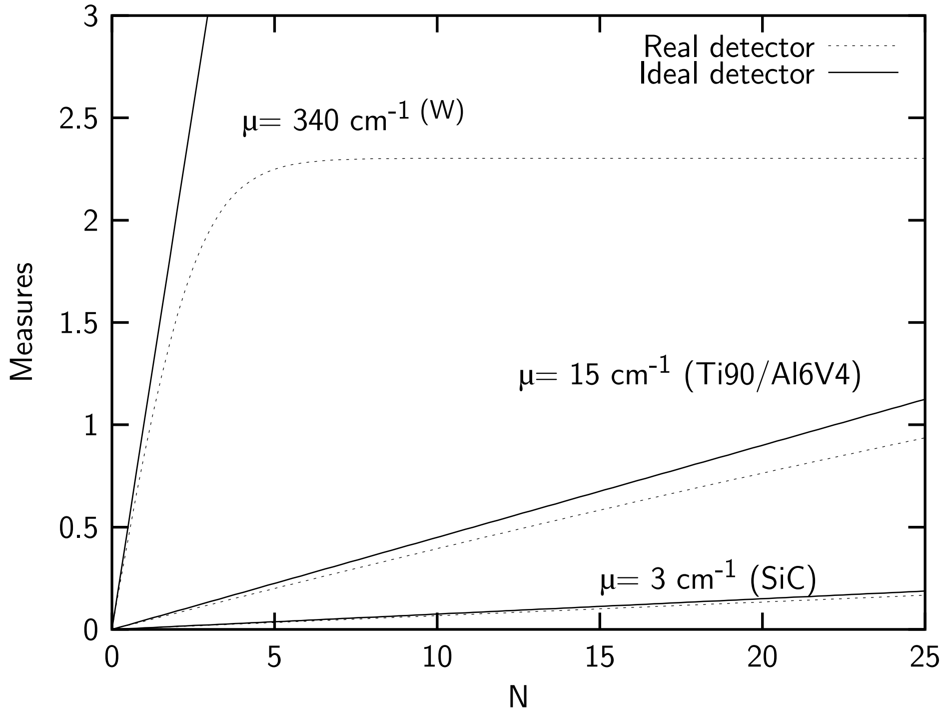

Figure 2.13: Example of measures given by a real and ideal detector. $k = 0.9$, $x = 0.003$ *cm (core size).*

To check the effect of the impulse response of the camera used at ESRF, the impulse response must be evaluated and it has to be applied in simulation with high density aligned samples. We will study it in the following subsections.

2.5.3 How to estimate the camera response

In subsection 2.5.2, we saw that the image is corrupted using a real detector when samples are aligned. Indeed the measures vary linearly in function of the crossed thickness using an ideal detector, which is not the case using a real one. To check the effect of a real detector onto tomographic reconstruction when high density materials are aligned, the impulse response of the detector has been experimentally estimated, then it has been used in simulation.

From the beginning of non-destructive testing (NDT), procedures for measuring and combining unsharpness were proposed. In 1946, Klasens proposed a such method [Kla46]. Criterion of his method is close to the British Standard [Bri88]. Total unsharpness is the following geometrical average:

$$h_{total} = \sqrt[n]{h_{inherent}^{n} + h_{geometric}^{n}} \tag{2.10}$$

with $h_{inherent}$ depending on CCD camera, converters and optics and $h_{geometric}$ depending on the distance of the sample to the source (according to Fig. 2.9, there is no geometry unsharpnesses in the case of parallel X-ray beams). For Klasens, n is equal to 3. But, if n is equal to 2, then unsharpness corresponds to a convolution by Gaussian functions [LP03].

Although the principle of the MTF measurement is simple and known for a long time, in practice it is not easy to deal with physical measurements. It comes from the difficulty to physically obtain an X-ray Dirac impulse. There are different methods for estimating the MTF. Most of them have been proposed for visible light imaging. In the case of X-ray imaging, four methods are commonly used [KZR+96, LP03]. To simplify, a linear detector (1D) is considered. There are:

1. The hole method:
   it consist in getting the image of a very small hole. The profile directly corresponds to the PSF.

2. The slit method:
   it is the same method as the hole method. The used object is very small slit. Thus, the line spread function (LSF) is directly obtained.

3. The bar/space pattern:
   a bar/space test object with increasing spatial density is used. Each section of the object corresponds to a periodic rectangular pattern. Contrast measurement of the pattern allows to evaluate the contrast transfer function (CTF).

4. The edge method:
   the test object is an edge. Thus, the profile corresponds to the edge spread function (ESF). The LSF is obtained by derivation of the ESF.

In practice, getting ESF is easier than getting directly impulse response (PSF). The unsharpness function is recovered via an edge signal derivation, sampled along the intensity gradient of a test object [LP03].

2.5.4 Getting the Edge Spread Function (ESF)

In the previous subsection, four methods to estimate the impulse response of the detector were presented. In practice ESF measurement is the easiest to perform. Therefore, we have decided to measure the detector response using this method. ESF depends on the used energy and the pixel size. To match the aluminium composite setup, the ESF has been estimated using 33 keV in energy and 1.9 μm pixel size. The response may be different in all direction. To check the isotropy of the response, several acquisitions are required. Considering acquisition duration, we have chosen to perform four different acquisitions as Fig. 2.14 shows.

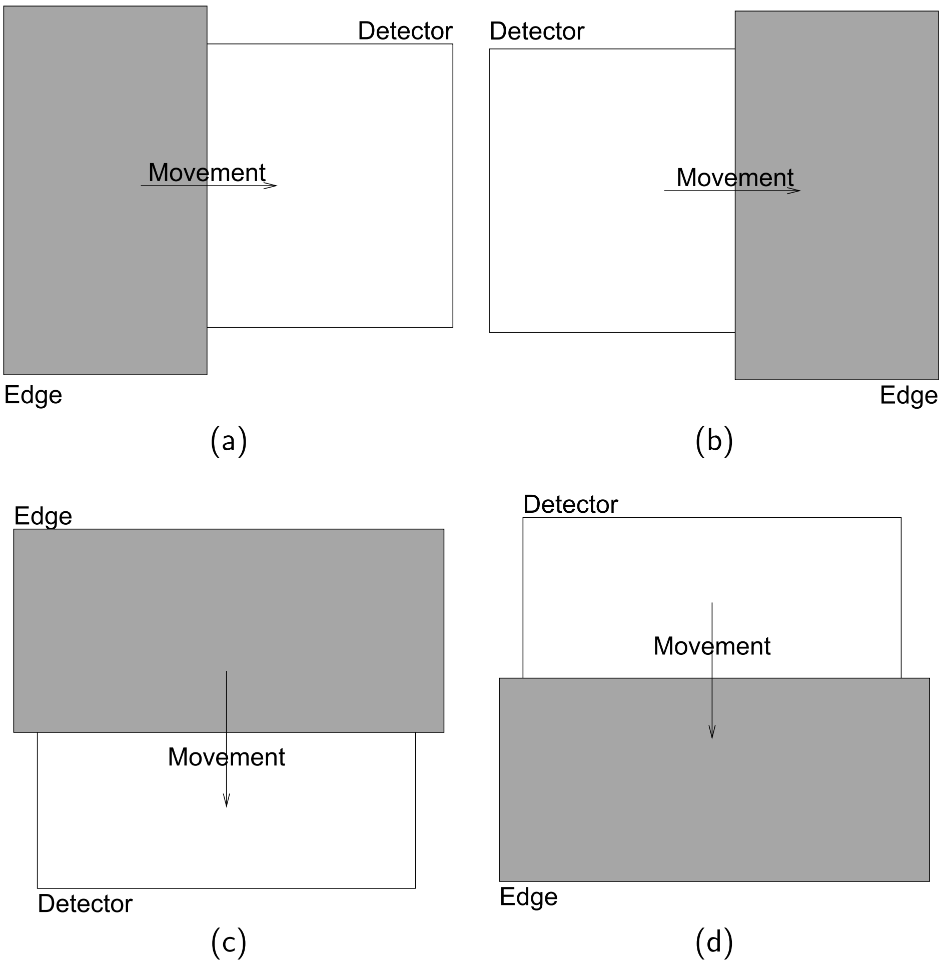

Figure 2.14: 4 acquisitions performed at ID19 ESRF beamline. 50 projections by acquisition. Synchrotron radiation, 33 keV in energy. (a) 1^{st} horizontal acquisition, (b) 2^{nd} horizontal acquisition, (c) 1^{st} vertical acquisition, (d) 2^{nd} vertical acquisition.

Edge material

Edge material has to be chosen carefully regarding:

- the possibility to get a very straight edge,

- the limitation of fluorescence and scattered photons.

To be accurate, as the pixel size is very small (1.9 µm), the edge must be very straight. To avoid degradation of information, scattering and fluorescence must be negligible comparing to directly transmitted photons.

Generally, edges are done from metal plates. But in our case (very small pixel size), it is difficult to machine an edge sufficiently straight. The chosen material is a gallium arsenide crystal (GaAs). When a plate of a gallium arsenide crystal is broken, the edge is very straight. The chosen GaAs crystal is a plate, 0.5 mm in thickness, which is quite big compared to pixel size.

As in subsection 2.2.3, a Monte Carlo simulation has been used to estimate the relative importance of each kind of photons (directly transmitted, scattered, fluorescence). The simulation has been carried out using GEANT4 with 33 keV in energy and a gallium arsenide crystal plate. 99.85% of the energy received by the detector behind the plate comes from directly transmitted photons. Other photons received by the whole detector represent 0,15% of the received total energy, among which:

Radiation	Percentage in received energy
Rayleigh (order 1)	98,92%
Compton (order 1)	0,05%
Multiple scattering (order 2)	1,02%
Multiple scattering (order 3)	0,01%
Multiple scattering (order > 3)	0,00%
Fluorescence & Bremsstrahlung	0,00%

Simulation results show that only directly transmitted photons are important. It proves that experimental data are not degraded by scattering and fluorescence because they are negligible.

Analysis of data

As fluorescence and scattered photons are negligible, data can be directly analyzed after flat field correction (for more details about flat field correction, see App. B).

Lack of samples The easiest way to obtain the ESF from one projection of an edge is to extract a profile. This method has not been performed due to lack of accuracy. Indeed, there are only few pixels along the intensity fall (Fig. 2.15). The resolution is too low. There are two ways to handle this lack of samples:

- The edge is moved along the intensity gradient direction [LP03, KZR$^+$96]. A pixel being hidden behind the object becomes 'visible'. Ideally, the motion span is at least equal to the unsharpness support. The step magnitude is computed to get the required number of sample.

- The test object has a long sharp edge, slightly twisted relatively to one line (or column) of the CCD. Therefore an oriented edge profile can be extracted with enough data points in the intensity fall. For more detail on oriented edge method, [LP03, Gv00] could be consulted.

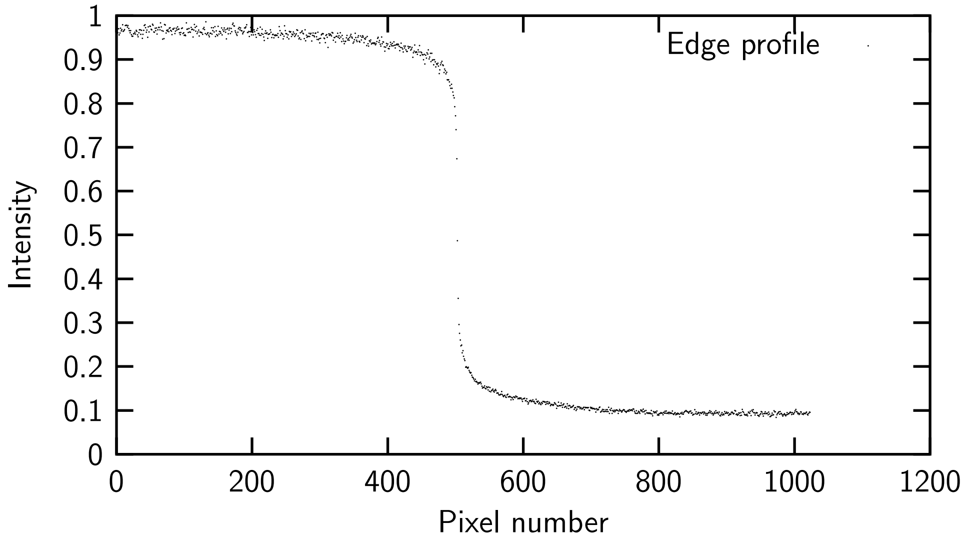

Figure 2.15: Profile of an edge obtained using a GaAs crystal, for the 2^{nd} horizontal acquisition. Synchrotron radiation, 33 keV in energy.

Generally, the second method is easier to carry out. Indeed, the edge is not supposed to be moved. But in the case of ID19 beamline, as samples can be accurately moved by engines controlled by computer, the first method has been used. The total edge displacement is approximately equal to 2.6 pixels (5 µm). Regarding the acquisition time, fifty projections of the edge have been performed by acquisition. So, between projections, the edge has been translated by a constant translation vector (0.1 µm).

Fig. 2.16 shows the intensity of different pixels (abscissas 500, 501 and 502) of the middle line for every projections of the second horizontal profile acquisition. Unfortunately, there are not enough data to reconstruct a whole profile using only intensities of one particular pixel. The displacement of the edge is too small. Meanwhile, it is possible to combine several extracted profiles at different pixel abscissas. By shifting the profiles, they can be readjusted. Indeed, a $pixel(x,y,t)$, with t the projection number, corresponds to a $pixel(x+1,y,t+k)$, with k equal to the pixel size divided by step ($\frac{1.9}{0.1}$). So, to readjust two successive profiles, one of them has to be shifted by 19 along the projection number axis, *e.g.* $pixel(501,512,5) \simeq pixel(502,512,24)$. However this theoretically translation vector has not been used.

Indeed to be more accurate, the translation vector has been estimated using experimental data. A mathematical function can fit profiles presented in Fig. 2.16. They have been fitted using the implementation of the nonlinear least-squares (NLLS) Marquardt-Levenberg algorithm of gnuplot. To approximate profiles, the used function is

$$f(x) = a + b \times \arctan((x-c)/d) \tag{2.11}$$

Profiles must be chosen taking onto account estimation errors. After fitting, gnuplot resumes the coefficients of Eq. 2.11 and estimation error rate. It is more accurate to determine parameters using profiles at pixels (501, 512) and (502, 512) than (500, 512). The difference of the c

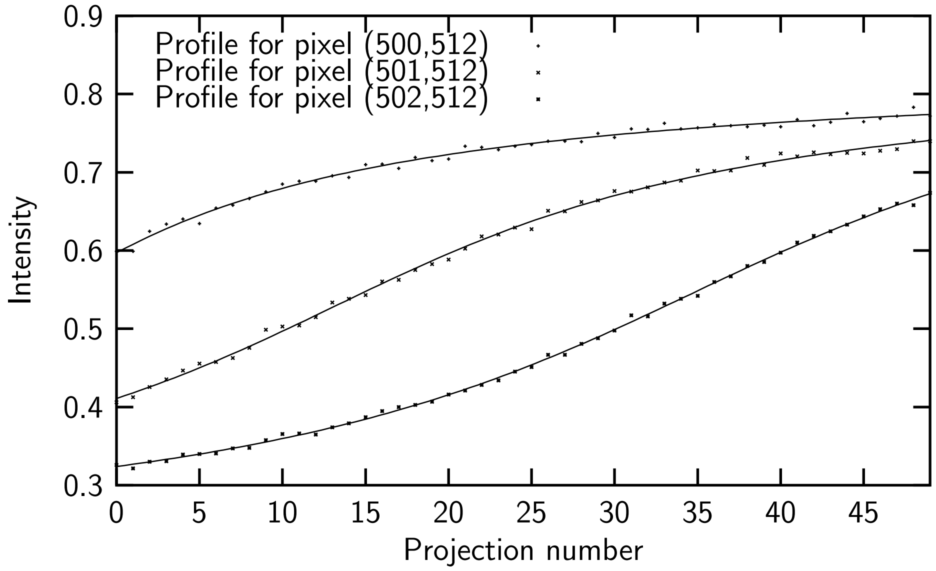

Figure 2.16: Extracted horizontal profiles for the 2^{nd} horizontal acquisition.

parameters between two successive profiles corresponds to the translation vector (in projection unit). gnuplot gives $c_{501} = 34.7209$ and $c_{502} = 13.1314$, then the translation vector is 21.5895 projections, which is not so far from the theoretical value. Fig. 2.17 shows a profile reconstructed by combining shifted profiles.

Lack of engines accuracy It has been found that the pitch of the edge movement is not really constant. Although the step has been set to 0.1 µm, it varies during the acquisition process. To deal with this inaccuracy problem, scaling factors have been applied to get all reconstructed profiles on the same scale. For each acquisition, the total edge displacement between the first and the last projections have been estimated using the the gnuplot fit function. It allows to get the average step used for each acquisition. Then scaling factors are deduced. Every reconstructed profiles are shown in Fig. 2.18. A better accuracy would be possible, if each step between two successive projections have been estimated. But it needs more computation time.

Fresnel reflection On Fig. 2.18, there are overshoots on the 1^{st} horizontal profile and the 2^{nd} vertical profile. They are probably due to Fresnel reflection. Incident beam has to be strictly perpendicular to the GaAs plate. Otherwise, Fresnel reflection occurs when the angle between incident beam and the edge is small. These two profiles were not usable to estimate the LSF. Moreover, it is to note that the 2^{nd} horizontal profile and the 1^{st} vertical profile are not probably completely right. Indeed, due to the large thickness of the plate comparing to the CCD pixel size, if incident beam and edge are not strictly perpendicular, then some pixels, which are not supposed to be covered by the plate, will be covered. As a consequence, the LSF will be probably over-estimated and the computed unsharpness will be greater than the real one.

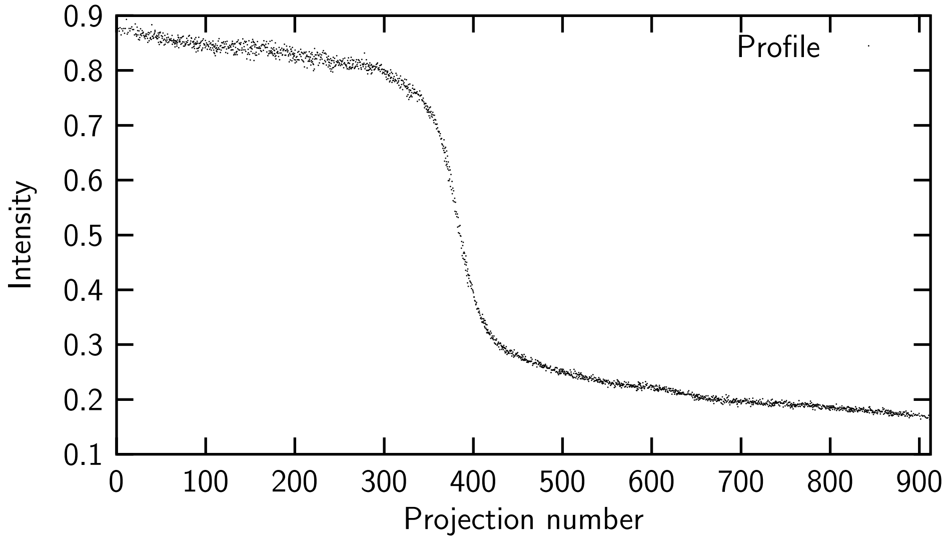

Figure 2.17: 2nd horizontal profile (ESF) after reconstruction.
Note: Comparing to profiles of Fig.2.16, the final reconstructed profile (Fig. 2.17) is vertically flipped. It allows to match this final reconstructed profile and the real one, which is already displayed in Fig. 2.15.

Fitting ESF by mathematical function In previous paragraphs, we described a method to reconstruct the profile of an edge. It corresponds to the ESF and characterizes the detector. By derivation of the ESF, the LSF is obtained. The LSF is an estimation of the impulse response of the detector. Using the gnuplot fit function, a mathematical function matches the ESF. The used function is formed as followed:

$$\mathrm{ESF}(x) = a + b \times \left(\arctan\left(\frac{x-c}{d}\right) + \mathrm{erf}\left(\frac{x-c}{e}\right)\right) \tag{2.12}$$

Fig. 2.19 illustrates functions, which match ESFs. App. C presents the different parameters computed by gnuplot for fitting the two set of data points.

Applying LSF From the ESF, the LSF is obtained by finite difference, together with a scaling factor (to get LSF in pixel unit).

Fig. 2.20 presents LSFs obtained from the estimated ESFs (Fig. 2.19). It shows that the impulse response of the detector is not isotropic. However, the two computed LSFs are quite close. But the tails of each estimated LSF spread onto at least 300 pixels, which is very important. To check the effect of the impulse response of the ID19 acquisition system, simulations have to be performed taking onto account this response.

In subsection 2.5.1, we saw that effect of impulse response is a convolution. Tomographic acquisitions have been simulated using ray-tracing with monochromatic radiation. All simulated projections are convolved by the LSF. Then a slice is reconstructed by tomography. Fig. 2.21

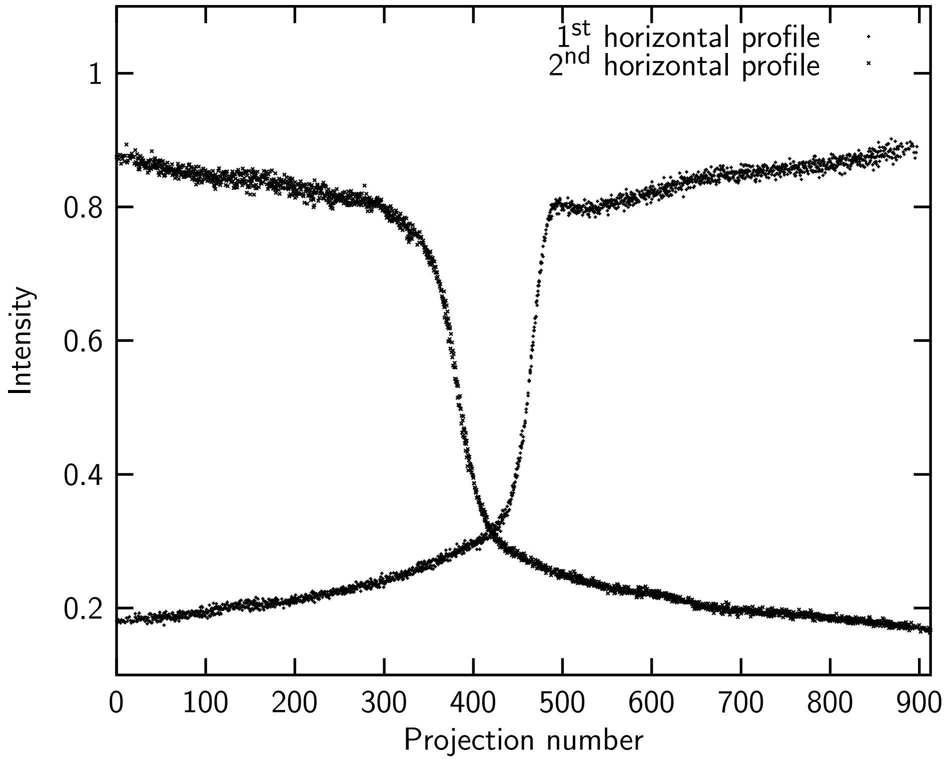

(a)

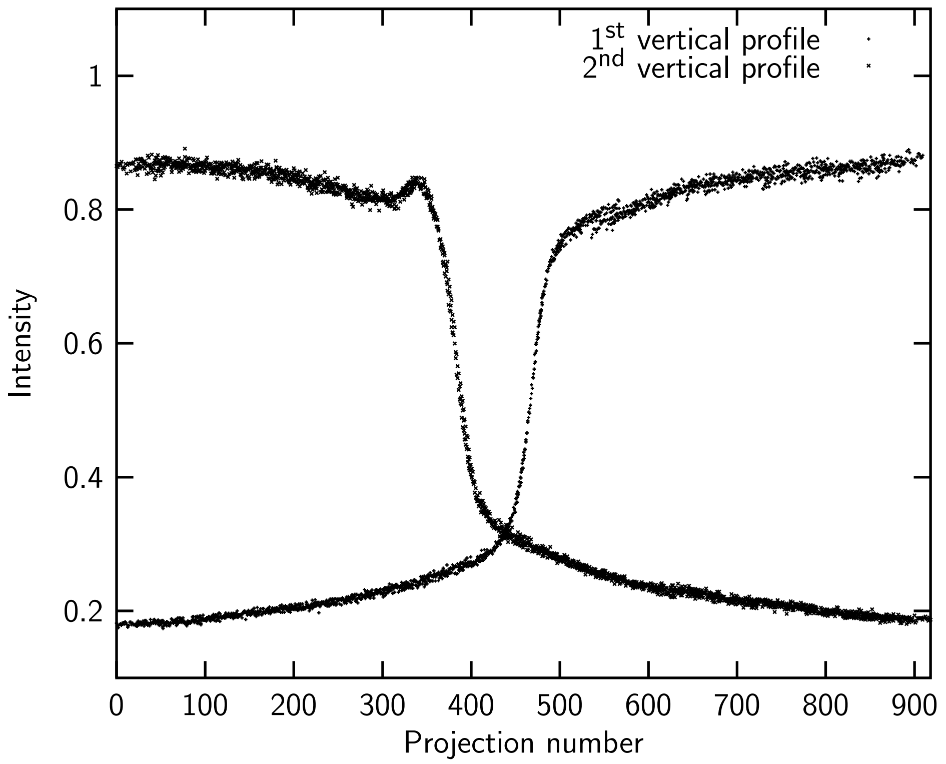

(b)

Figure 2.18: (a) reconstructed vertical profiles, (b) reconstructed horizontal profiles.

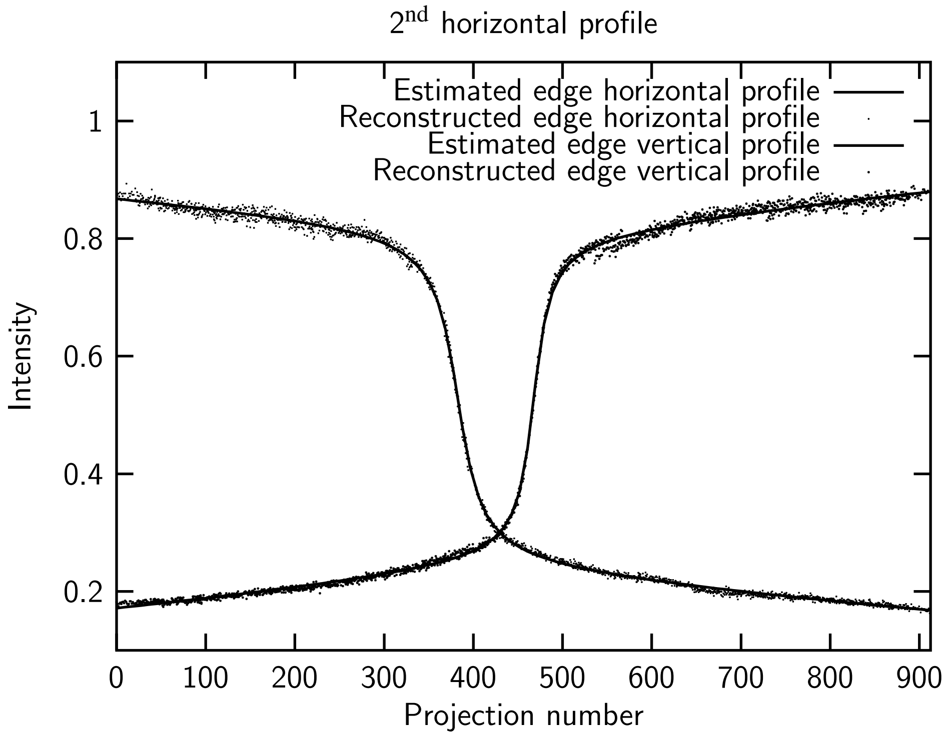

Figure 2.19: Estimated ESF.

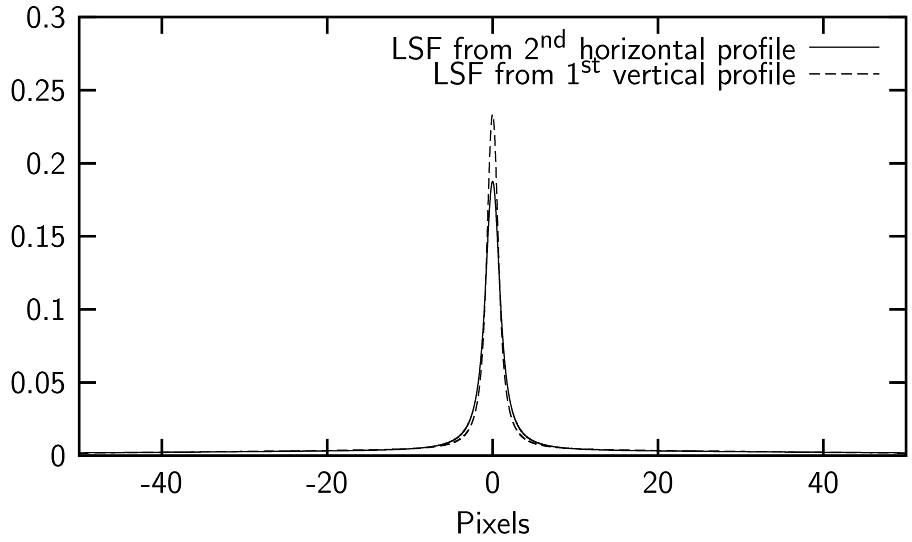

Figure 2.20: Estimated LSF.

is the result of a such simulation.

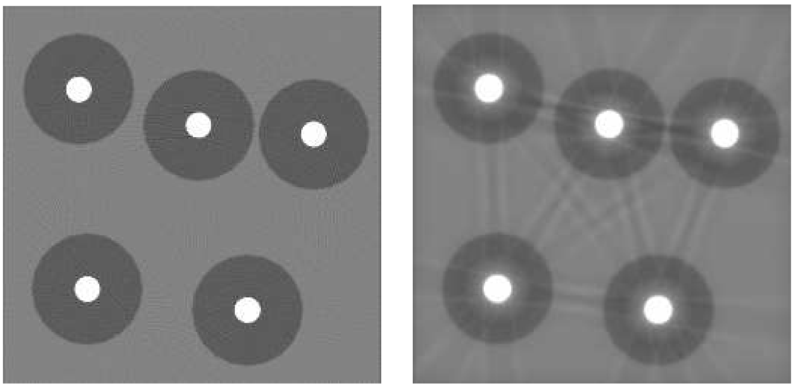

(a) (b)

Figure 2.21: Simulated tomographic slices. Monochromatic incident beam, 33 keV in energy. Distance between source and detector, 145 m (parallel photons beam). Distance between detector and sample, 80 mm. Pixel size 1.9 µm. 900 projections, angular span 180°. (a) simulation with an ideal detector. (b) simulation with a real detector (LSF estimated from 1st vertical acquisition).

The detector impulse response products artefacts in the reconstructed volume similar to those observed from experimental data.

2.6 Phase contrast

On tomographic slices obtained using experimental data (Fig. 2.1 & Fig. 2.3), phase contrast artefacts are observed (for more detail on phase contrast phenomena, see [Clœ99]). On these images, phase contrast artefacts correspond to dark and bright waves located at intensity edges. To check the effect of phase contrast combined with impulse response on tomographic slices, simulations have been carried out at ESRF, using Peter Clœtens' simulation software (Fig. 2.22, 2.23 & 2.24).

Images of Fig. 2.23 are simulated with phase contrast. The detector is considered as perfect (the impulse response is a Dirac impulse). Around tungsten and carbon cores, there are phase contrast artefacts (black and white rings). In both cases, there are also phase contrast artefacts around silicon carbide fibers. Considering a real detector (Fig. 2.24), phase contrast artefacts do not change much around fibers and the carbon core. But in the case of tungsten core, a real detector considerably reduces artefacts around the core. Simulation is in adequacy with reality, *i.e.* Fig. 2.25 (reality) is closer to 2.24 (simulation) than 2.23 (simulation).

To conclude, the effect of the combination of phase contrast and LSF is closer to reality than only the effect of phase contrast. It proves that the impulse response of the detector really plays a role into artefacts observed on slices using experimental data.

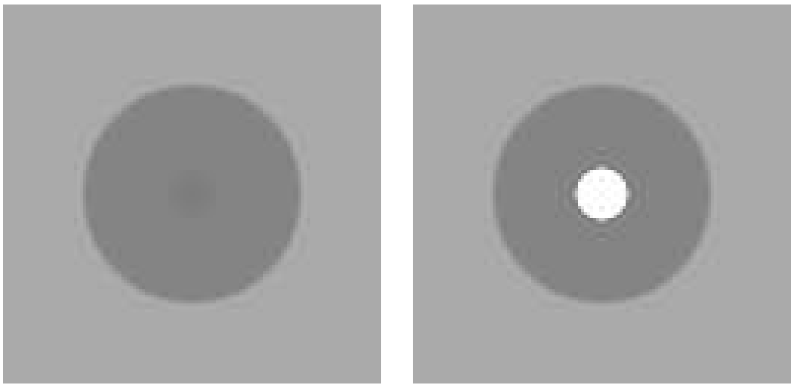

(a) (b)

Figure 2.22: Simulated tomographic slices. Ideal detector. No phase contrast simulated. Incident beam, 33 keV in energy. Distance between detector and sample, 80 mm. Pixel size 1.9 µm. 900 projections, angular span 180°. Matrix in Ti90Al6V4, Fiber in silicon carbide. (a) carbon core, (b) tungsten core.

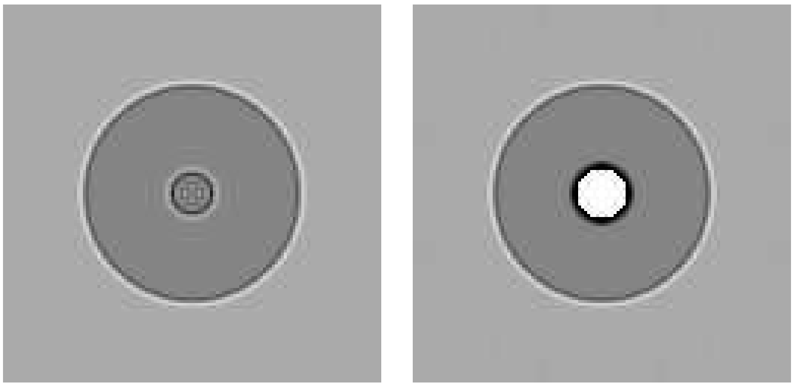

Figure 2.23: Similar parameters to Fig. 2.22. Simulation with ideal detector and phase contrast.

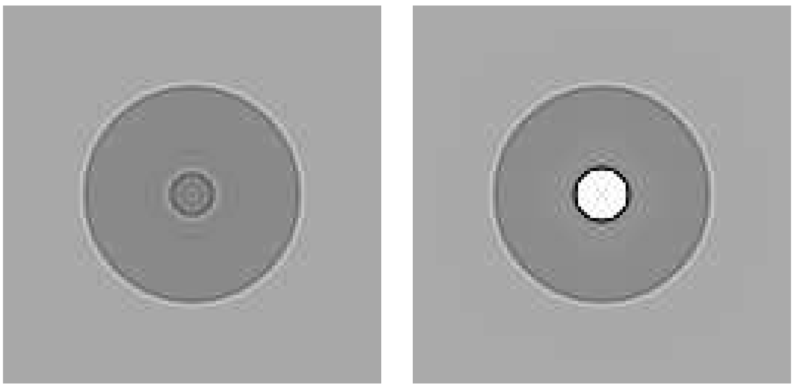

Figure 2.24: Similar parameters to Fig. 2.22. Simulation with real detector and phase contrast.

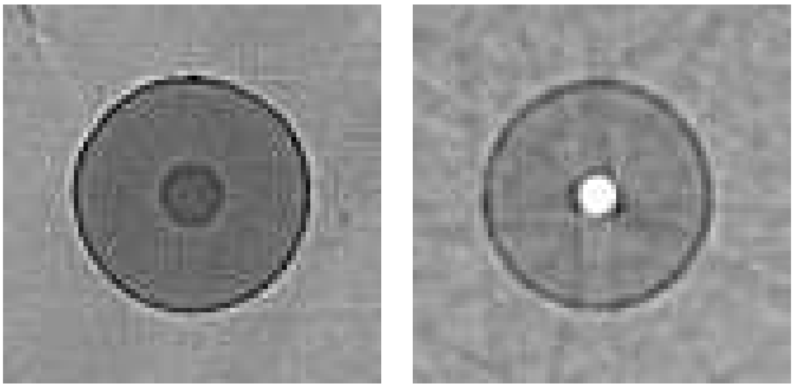

Figure 2.25: Extract of tomographic slices. Matrix in Ti90Al6V4, Fiber in silicon carbide. On left, core in carbon. On right, core in tungsten. Synchrotron radiation, 33 keV in energy. Distance between source and detector, 145 m (parallel photons beam). Distance between detector and sample, 80 mm. Pixel size 1.9 µm. 900 projections, angular span 180°.

2.7 Conclusion

On tomographic slices reconstructed using experimental data, there are artefacts when high density materials are aligned. Indeed, dark lines bordered by thin bright lines appear. In this section, two different causes of artefacts were revealed by simulation.

Only few harmonic components are sufficient to produce these dark line artefacts. This phenomena is known as beam-hardening.

Simulations of phase contrast with different setups have proved that the impulse response of the detector is present and plays a role in phase contrast artefacts production. The estimated detector impulse response can also generate dark line artefacts.

Then artefacts are probably due to the combination of few harmonic components and the detector response.

Chapter 3

Removing artefacts

In the previous section, we saw that harmonic components and detector response are accountable for dark line artefacts when high density material objects are aligned. The X-ray images are blurred by the detector (convolution by a low-pass filter), but since the reconstruction process is not linear (logarithm of the attenuation measures), it does not simply result in a blurred reconstructed tomographic slice.

Deconvolution consists in inverting the smoothing due to the convolution. Many methods have been proposed in the past to solve this problem [Clœ99, Cul94]. They can be linear or non-linear, blind or with a priori knowledge, direct or iterative. In the context of this study, the detector response being available by measurement, a supervised deconvolution is preferred to a blind one. We propose to solve this degradation problem by an iterative fixed point algorithm.

3.1 Basic idea

An iterative fixed point method is proposed to correct the effect of detector impulse response. The algorithm is implemented as an iterative function as follows:

Function: deconv
Parameters: *input*, the input image (observations); *kernel*, the convolution kernel; *nb_iteration*, the number of iteration.
Return: *output*.
Require: $nb\_iteration > 0$.
Ensure: *output*, result of the deconvolution.
Local variables: *i*, an integer; *output*, an image; *conv*, an image; *err*, an image.

```
i ← 1
output ← input
while i <= nb_iteration do
    conv ← convolution of output by kernel
    err ← input − conv
    output ← output + err
    i ← i + 1
end while
```

In App. D.1, you will find the deconvolution function and a test program applied to 1D signal. Fig. 3.1 shows the signal used for testing the algorithm. P_0 is the ideal signal. It is considered as unknown. P_1 is known, it simulates the measured signal, the result of the convolution of P_0 by the detector response.

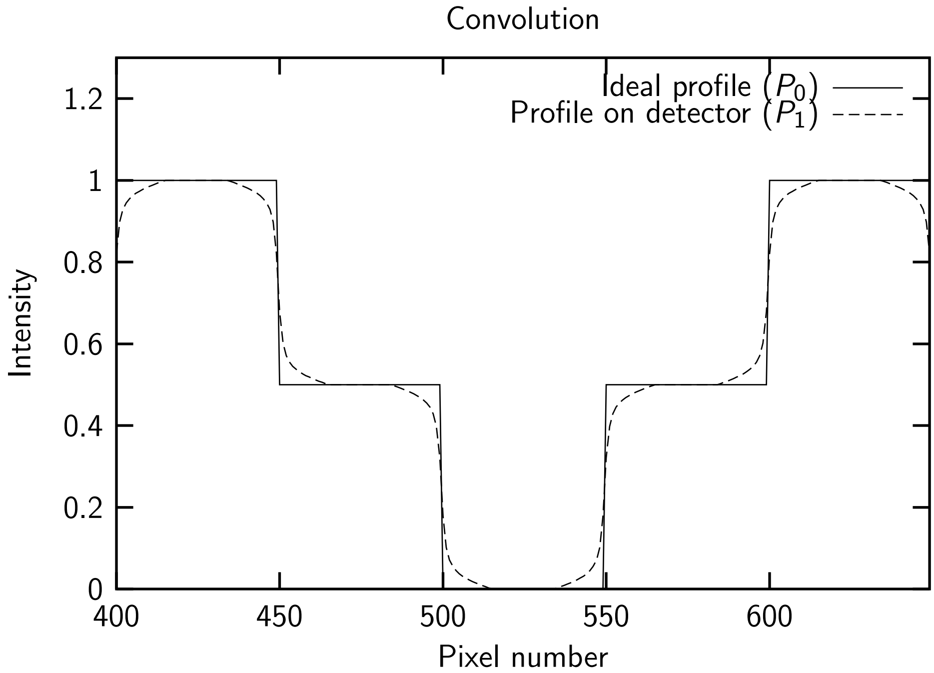

Figure 3.1: Simulated profiles. The ideal profile is convolved by the LSF estimated from the 1st vertical acquisition.

Fig. 3.2 illustrates the result (P_1') of the deconvolution algorithm on P_1 at the 1st iteration. To get a better result and to check the evolution of the result through iterations, we increase the number of iterations. Fig. 3.3 shows results until the 3rd iteration. The result is closer to the ideal profile.

We have got a satisfying result by deconvolution with the right kernel. But in practice, the kernel is estimated from experimental data. The estimation can differ from the real one. To determine the stability of the algorithm regarding on the deconvolution kernel, a profile convolved by a LSF is deconvolved using another one. Figures 3.4 and 3.5 show that the kernel used in the deconvolution is influent. Indeed, high frequencies can be reduced or increased. The experimental estimation of the response of the detector is therefore a very sensitive issue.

We have seen how to remove errors using an iterative deconvolution algorithm, in the next section, this algorithm will be adapted to X-ray tomography.

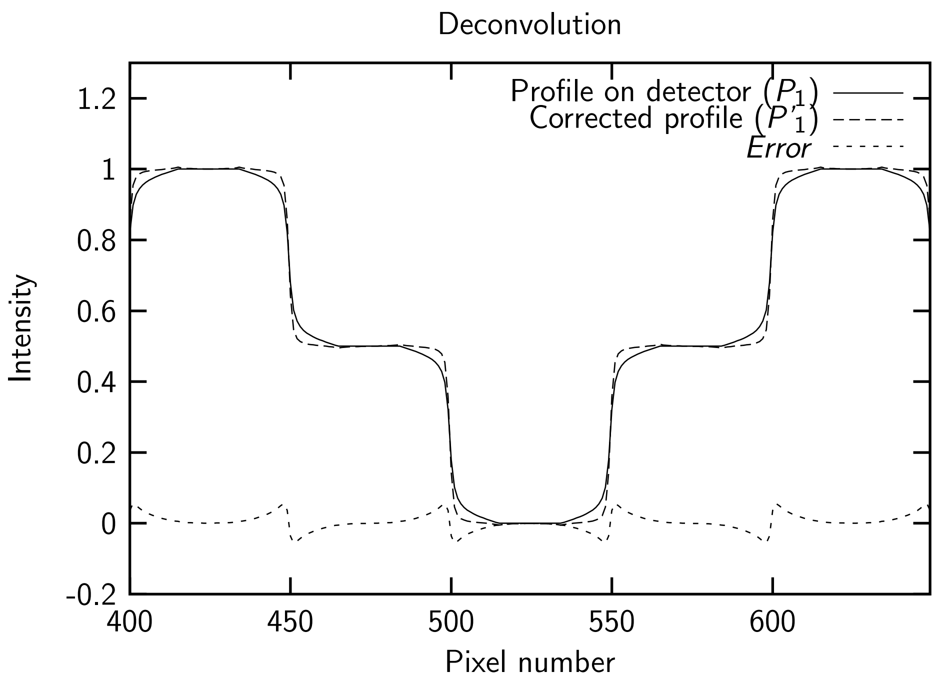

Figure 3.2: Simulated profiles. Deconvolution at the 1st iteration.

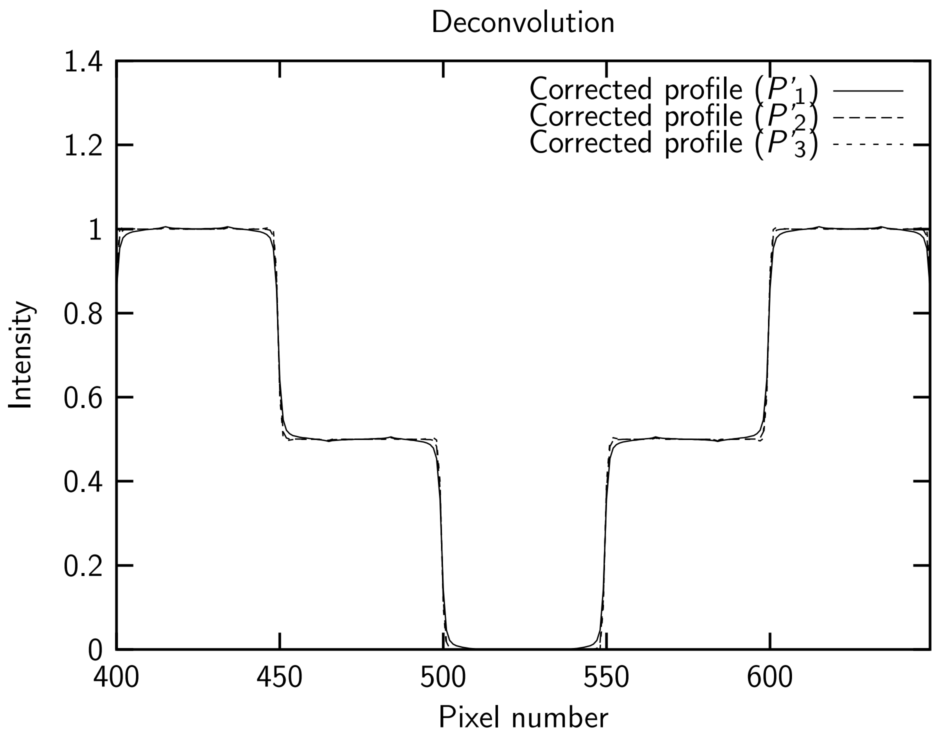

Figure 3.3: Evolution through iterations. 1st, 2nd and 3rd iterations.

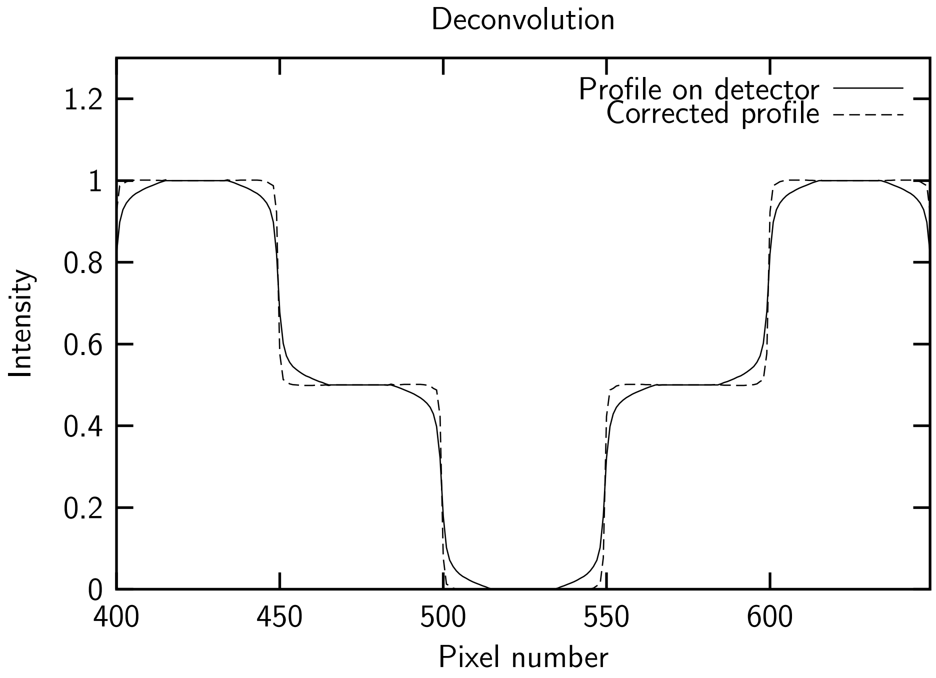

Figure 3.4: Profile simulated with LSF from the 2^{nd} horizontal acquisition. Profile corrected at the 19^{th} iteration using LSF from 1^{st} vertical acquisition.

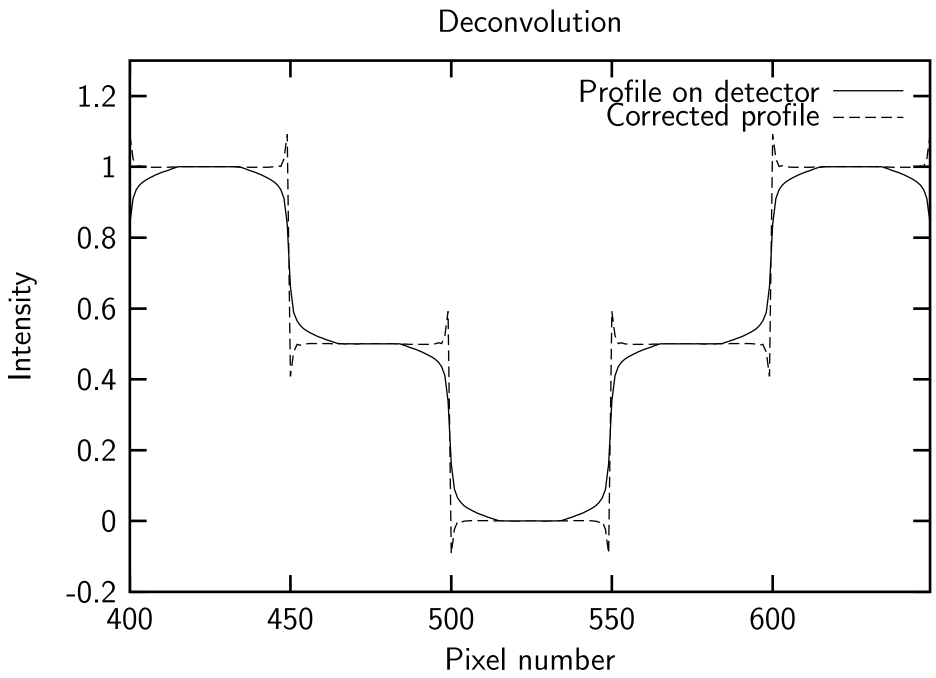

Figure 3.5: Profile simulated with LSF from the 1^{st} vertical acquisition. Profile corrected at the 19^{th} iteration using LSF from 2^{nd} horizontal acquisition.

3.2 Removing artefacts in simulated tomographic slices

In the previous section, an iterative deconvolution algorithm was proposed to improve data. In this part, this algorithm will be adapted to X-ray tomography. In simulation context, the iterative fixed point algorithm becomes:

1. Tomographic acquisition simulation using the original version of VXI.
   From CAD files, projections are simulated.

2. Simulation of impulse response of the detector.
   Convolution of every projections by the estimated impulse response of the detector.

3. Tomographic reconstruction of a slice.
   From convolved projections, a tomographic slice is reconstructed.

4. Tomographic acquisition simulation from the reconstructed slice.
   μ map is used as voxels[1] *using a modified version of VXI.*

5. Simulation of impulse response of the detector.
   Convolution of new projections by impulse response of the detector.

6. Getting difference.
   Subtraction of original sinogram by the new convolved sinogram.

7. Getting errors map.
   Tomographic reconstruction of the difference.

8. Getting corrected slice.
   Adding difference to the previous reconstructed slice.

9. Repeat operations from (4.) using this new slice.

The whole algorithm has been implemented using a Bourne-Again SHell (Bash) script. Each step of this algorithm corresponds to an individual C or C++ image processing program, *i.e.* there is a program for the initial simulation (step 1.), a program for the convolution (steps 2. and 5.), etc. In App. D.2, a schema presents the implementation of the algorithm, with every different program calls and input/output files.

In subsection 1.4.2, the simulation toolkit VXI was presented. It is noted that it uses 3D polygon meshes to set samples geometry. A material is assigned to each sample (*e.g.* tungsten or carbon). But in this part, the correction algorithm iterates using reconstructed tomographic slices as input data. Slices are similar to μ cartographic images, *i.e.* a pixel of a 2D slice or a voxel of a 3D volume corresponds to a linear attenuation coefficient at a given energy: the correction algorithm has to deal with voxels characterized by their corresponding linear attenuation coefficient. Considering the study duration, developing a new simulation toolkit dedicated to voxel representation is too ambitious. A new version of VXI has been designed to deal with voxels.

[1]VOlume ELement

In fact each pixel of an input slice is represented by a cube defined by a polygon mesh (12 triangles) and a μ. The radiographic images are then computed directly using the Beer-Lambert law with these μ values.

Fig. 3.6 illustrates the result of the algorithm on a tomographic slice simulated with artefacts. A tomographic acquisition of a step made of tungsten is simulated taking into account the impulse response of the detector. Then, using the iterative algorithm, the slice is corrected.

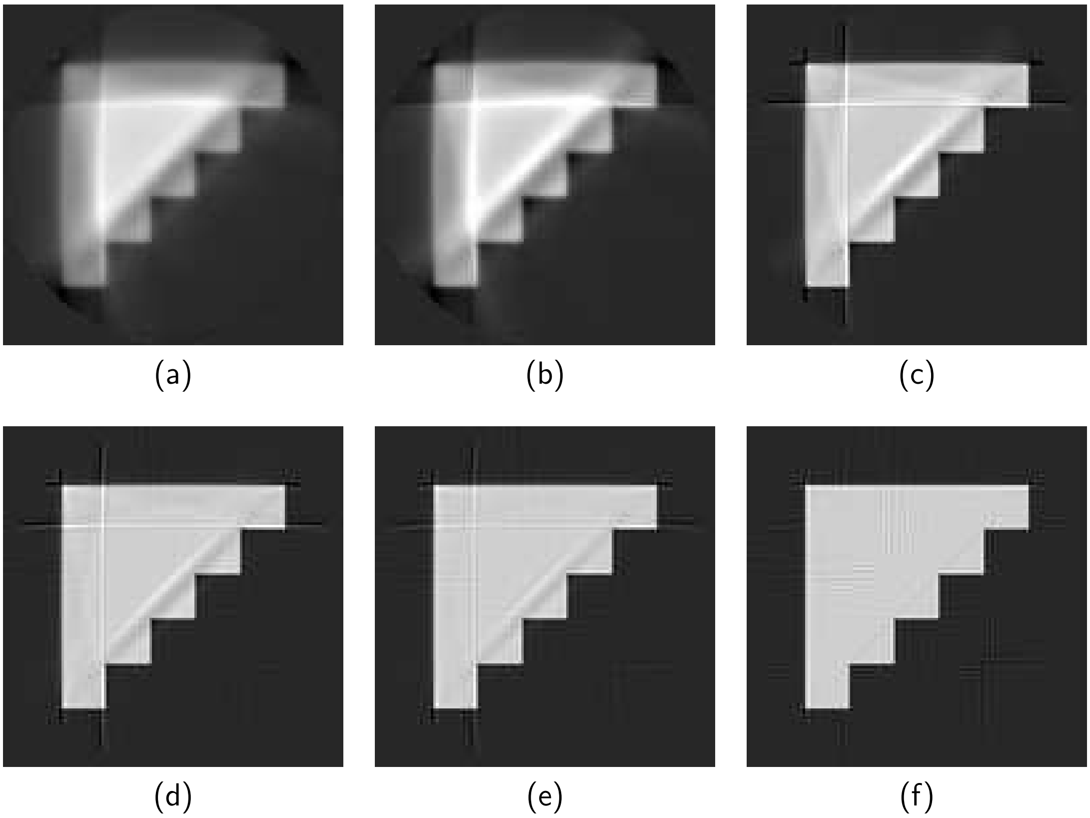

Figure 3.6: Correction of simulated artefacts. Slice size: 128 ×128 in pixels. Computing time: less than 3 minutes by iteration. (a) initial slice, (b) 1st iteration, (c) 10th iteration, (d) 20th iteration, (e) 30th iteration, (f) 100th iteration.

Fig. 3.7 illustrates the result of the same algorithm onto another simulation. A tomographic acquisition of a sample made of W cores, SiC fibers and a Ti90Al4V6 matrix is simulated taking into account the impulse response of the detector. Then, using the iterative algorithm, the slice is corrected.

The algorithm converges faster for the second illustration than for the first. In the first case, artefacts are more important because of a very accurate alignment of stairs, whereas in the second case tungsten cores are not strictly aligned.

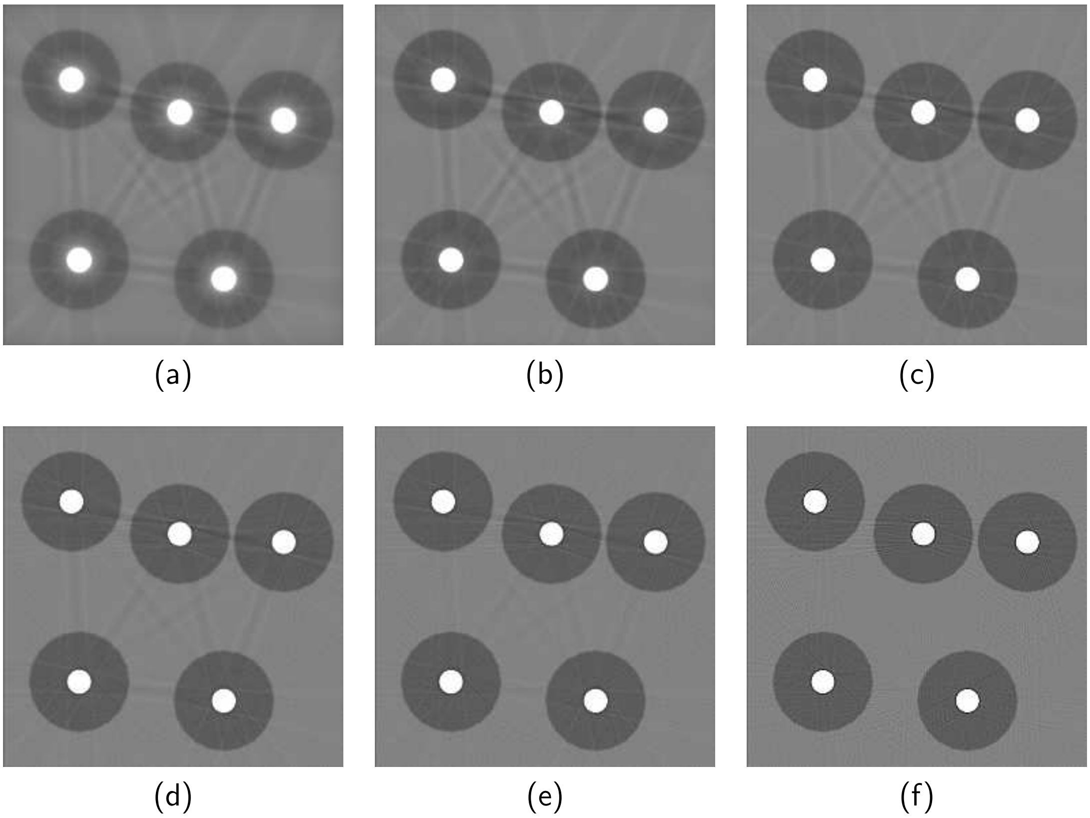

Figure 3.7: Correction of simulated artefacts. Slice size: 480 ×480 in pixels. Computing time: about 1.5 hour by iteration.(a) initial slice, (b) 1^{st} iteration, (c) 2^{nd} iteration, (d) 3^{rd} iteration, (e) 4^{th} iteration, (f) 10^{th} iteration.

The rendering time of an iteration is higher for the second simulation because slices are bigger. In the third chapter of Nicolas Freud's PhD thesis [Fre03], the complexity of the computing algorithm of VXI is introduced. We can consider that the complexity of the original algorithm is $O(n)$, with n the number of pixels of the virtual detector. In the case of the modified algorithm, which deals with voxel data, there are as many original simulations as there are voxels. In a slice, there are m^2 voxels, with m the edge size of a slice in pixel (the edge size can differ from the virtual detector size due to scaling factor). Therefore the algorithm complexity becomes $O(m^2)$.

3.3 Testing using experimental data

In the previous section, the fixed point algorithm was adapted to x-ray tomography. Some tests on data obtained by simulation were successfully performed. Here, we will see what is happened using experimental data.

The LSF has been estimated using a complex algorithm to avoid a lack of data and engines inaccuracy. Inevitably, there is numerical inaccuracy. Moreover the LSF is probably over-estimated and we have got two different kernels, the first is horizontal and the second is vertical. The first step is to tune them to get the better convolution kernel to remove artefacts. By changing the scale of the kernel, we can try to deconvolute the profile shown in Fig. 2.15. Indeed, the ideal profile of the sample is perfectly known. Fig. 3.8 illustrates the result of the algorithm with different kernels. No kernel is able to deconvolute perfectly the signal. A kernel with a short size does not compensate the effect of the impulse response. But a kernel with high size produces overshoots. We will use the one which match the more the ideal profile.

The last step is to run the algorithm using a tuned kernel and experimental data. Fig. 3.9 shows the result of the iterative fixed-point algorithm adapted to x-ray tomography. The used kernel is the one estimated from horizontal LSF and scale by 0.5. Using real data, the artefacts are removed slowly comparing to the use of simulated data. The width of dark lines becomes shorter. It removes blur and adds some noise. Fig. 3.10 illustrates that corrected attenuation coefficients are closer to theoretical values than initial coefficients. Unfortunately, dark line artefacts are still visible. Two different causes are possible:

1. the amount of harmonic components has not been evaluated, then removing harmonic effect has not been managed in this study,
2. the used convolution kernel to deconvolute the signal is not strictly right.

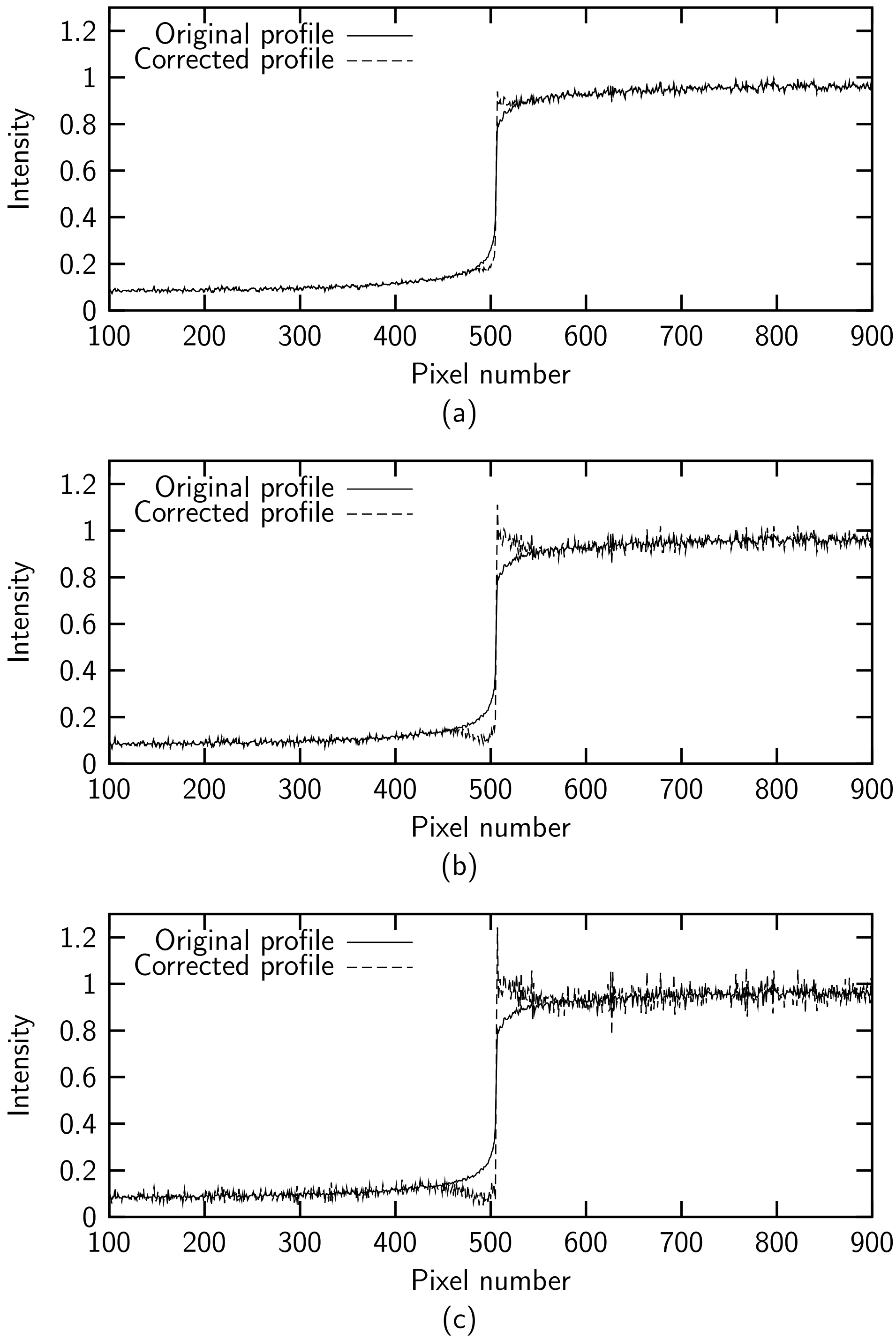

Figure 3.8: Tuning the convolution kernel size. Original kernel size, 301 pixel. (a) kernel scaled using factor 0.25, (b) kernel scaled using factor 0.5, (c) kernel scaled using factor 0.67.

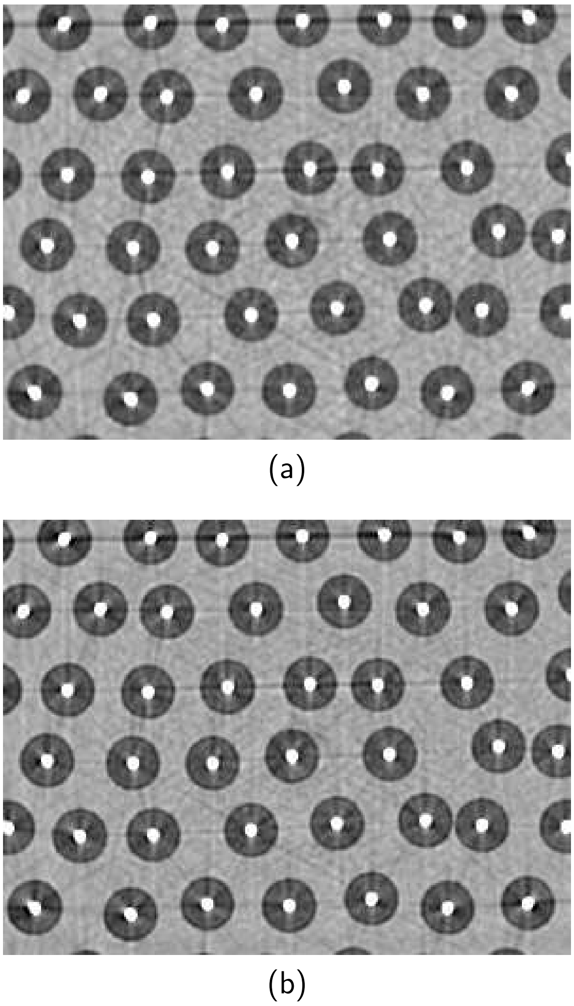

Figure 3.9: Region Of Interest of a slice of the aluminium composite reconstructed from experimental data. (a) initial slice, (b) 21th iteration.

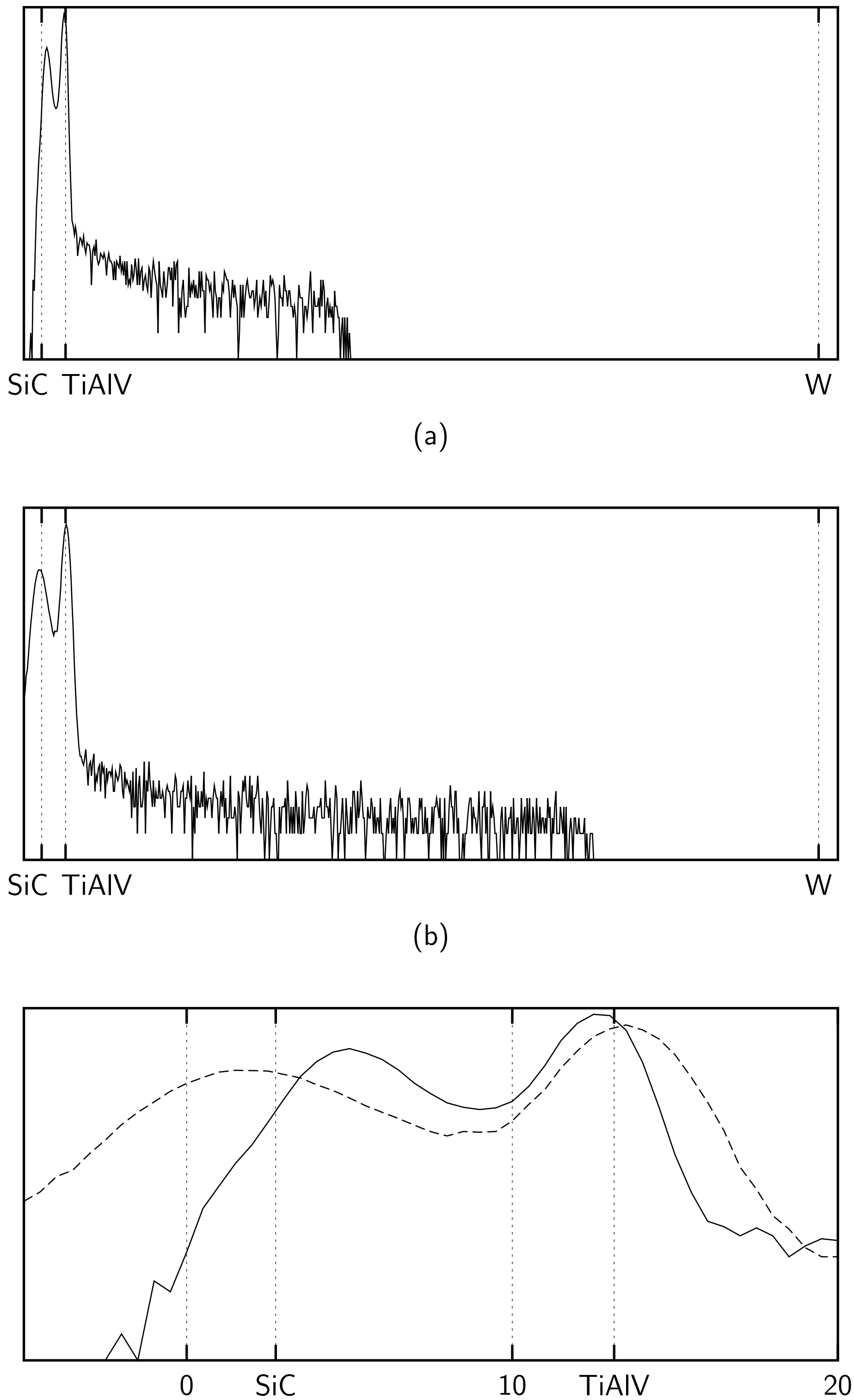

Figure 3.10: Histogram of reconstructed slices. (a) Initial slice, (b) 21th iteration. (c) Zoom between gray intensities -0.5 and 20.

Conclusion

This project was proposed by Jean-Michel Létang and Gilles Peix of CNDRI Lab. The basic idea of this study comes from the disclosure of strong artefacts in specific micro-tomographic volumes acquired at ESRF on ID19 beamline by Professor Jean-Yves Buffière and Dr Eric Maire of GEMPPM. Indeed some dark lines appear when high density objects are aligned.

After introducing briefly X-ray imaging in chapter 1, we determined in chapter 2 the origin of these dark-line artefacts using both simulation tools and real experiments. Then in chapter 3, a method was proposed to removed artefacts due to impulse response of the detector.

The exhaustive study of possible artefact origins was carried out. Two different causes have been highlighted:

- **By ray-tracing simulation, few harmonic components are sufficient to generate similar dark line artefacts**.
- To check the effect of the impulse response of the FRELON camera, the Edge Spread Function (ESF) of the whole acquisition system has been partially estimated. However, we show by simulation that **the estimated response is also accountable for producing dark line artefacts**.

Phase contrast simulations have proved that the impulse response of the acquisition system is really accountable. Consequently, <u>dark-line artefacts result from the combination of few harmonic components and the detector response</u>.

Simulated artefacts caused by the detector response have been successfully removed using a method adapted from the fixed point iterative algorithm applied to X-ray tomography. However, we saw that the fixed point algorithm is sensitive during the deconvolution process to the estimated impulse response.

Unfortunately, the algorithm has not been sufficiently tested on experimental data because of a lack of time. Indeed, the estimated ESF is probably over-estimated. So, the use of this algorithm on experimental data need more time to tune the PSF.

In the future, some work could be performed to complete this current study:

- the impulse response should be more accurately estimated. The lack of data and engines inaccuracy imply a complex algorithmic solution. Consequently, there are many computations, which also generate inaccuracy. To avoid the part of this problem due to a lack of data, more data have to be acquired to minimize calculation. It will need more time at ESRF.

- More acquisition time will also allow to check the isotropy of the response of the system.

- The correction of harmonic components should be studied. The amount of harmonic components has to be accurately estimated. Anyway, managing the harmonic components of synchrotron radiation only occur when high density samples are aligned. It can be done by software (calibration or heuristically during the deconvolution process). Another possibility is maybe to use another monochromator, which will reduce the number of harmonics, but it will also increase the acquisition time. A such monochromator can be used only in the case of high density material alignment.

- To test the algorithm onto real data, another set of projections will have to be acquired. Indeed, provided data were quite old and some parameters were missing, *e.g* the used monochromator. Ideally, all these acquisitions, projections for tomography, projections of a GaAs plate, etc. should be acquired in the same time.

- We can also imagine a protocol to validate the estimated PSF, *e.g.* acquiring a projection of a simple sample with a known ideal profile and trying to deconvolute the profile tuning the PSF until convergence to the ideal profile. This projection can be the plate made of GaAs. If the new estimated PSF is not isotropic, it should be tested using different orientation of the plate.

- To correct artefacts, other deconvolution methods should be tested. A benchmark will compare other methods to the one proposed in this study.

- Another possibility to correct the impulse response can be an hardware solution, by modifying the acquisition system. Indeed a discussion after a presentation of this study at ESRF, has shown that the screen (X-ray to visible light converter) is very thin and has to be supported near the CCD. The thickness of the support is quite big. In it, there can be scattering, which increases the PSF tails.

Bibliography

[Ama00] K. Amako. Present status of geant4. Nuclear Instruments and Methods in Physics Research A, pages 455–460, 2000.

[AR68] F.H. Attix and W.C. Roesch. Radiation dosimetry, chapter x-ray and γ-ray interactions. Academic press, 2nd edition, 1968.

[BCL02] A. Bonin, B. Chalmond, and B. Lavayssière. Monte-carlo simulation of industrial radiography images and experimental desings. NDT&E International, pages 503–510, 2002.

[BH87] M.J. Berger and J.H. Hubbell. XCOM: Photons cross sections on a personal computer. Technical Report 87-3597, NBSIR, 1987.

[BHS$^+$99] M.J. Berger, J.H. Hubbell, S.M. Seltzer, J.S. Coursey, and D.S. Zucker. Xcom: Photon cross section database (version 1.2). Online database, NIST, 1999. Accessible at: `<http://physics.nist.gov/PhysRefData/Xcom/Text/XCOM.html>`, visited the 5th December 2002.

[Ble93] J.P. Blewett. R.R. Wilson prize lecture: Advantures with accelerators. In Particle Accelerator Conference. IEEE, 1993.

[BP02] H. Benali and F. Peyrin. La tomographie - Fondements mathématiques, imagerie microscopique et imagerie industrielle, chapter Les méthodes discrètes. LAVOISIER, 2002.

[Bri88] British Standards Institution. BS 6932, Measurement of the effective focal spot size of mini-focus and microfocus X-Ray tubes used for industrial radiography, 1988.

[Cen98] E. Cendre. Tomographie à haute résolution par rayons X, application à l'étude de la perte osseuse chez le sujet âgé. PhD thesis, Institut National des Sciences Appliquées de Lyon, 1998.

[CHK97] D.E. Cullen, J.H. Hubbel, and L. Kissel. Epdl97: the evaluated photon data library, ´97 version. Technical report, Lawrence Livermore National Laboratory, 1997.

[Clœ99] P. Clœtens. Contribution to Phase Contrast Imaging, Reconstruction and Tomography with Hard Synchrotron Radiation. PhD thesis, Vrije Universiteit Brussel, 1999.

[Cor03a] Goodfellow Corporation. Material information silicon carbide. Online database, 2003. Accessible at: <http://www.goodfellow.com/csp/active/static/E/SI67.HTML>, visited the 12th December 2002.

[Cor03b] Goodfellow Corporation. Material information titanium/aluminium/vanadium. Online database, 2003. Accessible at: <http://www.goodfellow.com/csp/active/static/E/TI01.HTML>, visited the 12th December 2002.

[CP02] A.-M. Charvet and F. Peyrin. La tomographie - Fondements mathématiques, imagerie microscopique et imagerie industrielle, chapter La tomographie synchrotron. LAVOISIER, 2002.

[Cul94] J.-C. Culioli. Introduction à l'optimisation. Ellipses, 1994.

[DFK+00] P. Duvauchelle, N. Freud, V. Kaftandjian, G. Peix, and D. Babot. Simulation tool for x-ray imaging techniques. In X-Ray Tomography in Material Science, pages 127–136. HERMES Science Publications, 2000.

[DFKB00] P. Duvauchelle, N. Freud, V. Kaftandjian, and D. Babot. A computer code to simulate x-ray imaging techniques. Nuclear Instruments and Methods in Physics Research B, pages 245–258, 2000.

[DG02] M. Defrise and P. Grangeat. La tomographie - Fondements mathématiques, imagerie microscopique et imagerie industrielle, chapter Les méthodes analytiques. LAVOISIER, 2002.

[ESR03] Inside the storage ring. Online documentation, 2003. Accessible at: <http://www.esrf.fr/AboutUs/GuidedTour/StorageRing>, visited the 11th June 2003.

[Fre03] N. Freud. Modélisation et simulation de système d'imagerie par rayons X et gamma. PhD thesis, Institut National des Sciences Appliquées de Lyon, 2003.

[FvFH97] J. Foley, A. van Dam, S. Feiner, and J. Hughes. Computer graphics: principles and practice. Addison-Wesley, 2nd edition in C, 1997.

[Gv00] P.B. Greer and T. van Doorn. Evaluation of an algorithm for the assessment of the mtf using an edge method. Medical Physics, pages 2048–2059, 2000.

[GW77] R.C. Gonzalez and Paul Wintz. Digital Image Processing. Addison-Wesley Publishing Company, 1977.

[Hol96] G. Holst. CCD Arrays, cameras, and displays. JCD Publishing and SPIES PRESS, 1996.

[Hou73] G.N. Hounsfield. Computerized transverse axial scanning (tomography): Part 1. description of system. Br J Radiol, pages 1016–1022, 1973.

[ID103] Id19 detectors. Online documentation, 2003. Accessible at: `<http://www.esrf.fr/exp_facilities/ID19/homepage/id19detectors.htm>`, visited the 11th June 2003.

[Kla46] H.A. Klasens. Measurement and calculation of unsharpness combinations in x-ray photography. Technical report, Philips Research Laboratories, 1946.

[KS88] A. Kak and M. Slaney. Principles of Computerized Tomographic Imaging. IEEE PRESS, 1988.

[KZR+96] V. Kaftandjian, Y.M. Zhu, G. Rozière, G. Peix, and D. Babot. A comparison of the ball, wire, edge, and bar/space pattern techniques for modulation transfer function measurements of linear x-ray detectors. Journal of X-Ray science and technology, pages 205–221, 1996.

[Lec02] G. Lecomte. Apport de la simulation pour la segmentation d'images rayons x de pièces de fonderie. Master's thesis, Institut National des Sciences Appliquées de Lyon, 2002.

[LFP03] J.-M. Létang, N. Freud, and G. Peix. Optimal calibration via virtual x-ray imaging for dual-energy techniques: appliction to glass wool. In Quality Control by Vision, pages 422–432. The society of Photo-Optical Instrumentation Engineers, 2003.

[LP03] J.-M. Létang and G. Peix. On-line x-ray focal spot assessment based on deconvolution using standart imaging devices. NDT&E International, pages 303–317, 2003.

[MB00] E. Maire and J.-Y. Buffière. X-ray tomography of aluminium foams and ti/sic composites. In X-Ray Tomography in Material Science, pages 121–125. HERMES Science Publications, 2000.

[Pey03] F. Peyrin. Tomographie. DEA Images & Systèmes, lesson of tomography, 2003.

[Ret98] F. Retraint. Contrôle non destructif de pièces industrielles par radiographie: caratérisation 3D à partir d'un nombre limité de vues. PhD thesis, Institut National des Sciences Appliquées de Lyon, 1998.

[SFAS01] F. Salvat, J.M. Fernández-Varea, E. Acosta, and J. Sempau. PENELOPE: A Code System for Monte Carlo Simulation of Electron and Photon Transport. Nuclear Energy Agency, OECD, 2001. Workshop Proceedinds, Issy-les-Moulineux, France, 5-7 Novemeber 2001, 234p.

[Wat00] A. Watt. 3D Computer Graphics. Addison-Wesley, 3rd edition, 2000.

[Wil96] E.J.N. Wilson. Fifty years of synchrotrons. In EPAC, 1996.

[WND+97] M. Woo, J. Neider, T. Davis, D. Shreiner, and OpenGL Architecture Review Board. OpenGL(R) Programming Guide: The Official Guide to Learning OpenGL, Version 1.2. Addison-Wesley, 3rd edition, 1997.

Appendix A

Testing the scaling factor in GEANT4

Fig. A.1 and A.2 are obtained by simulations using GEANT4 with the setup presented in Sec. 2.2.2. The purpose was to check that X-ray simulations remain the same when all geometrical dimensions are scaled inversely to the material densities. Simulations use a fan beam, 400 keV. An iron box of $100 \times 100 \times 50$ in mm, with a cavity of $20 \times 5 \times 2.5$ in mm was placed in front of a lead filter ($300 \times 300 \times 1$ in mm).

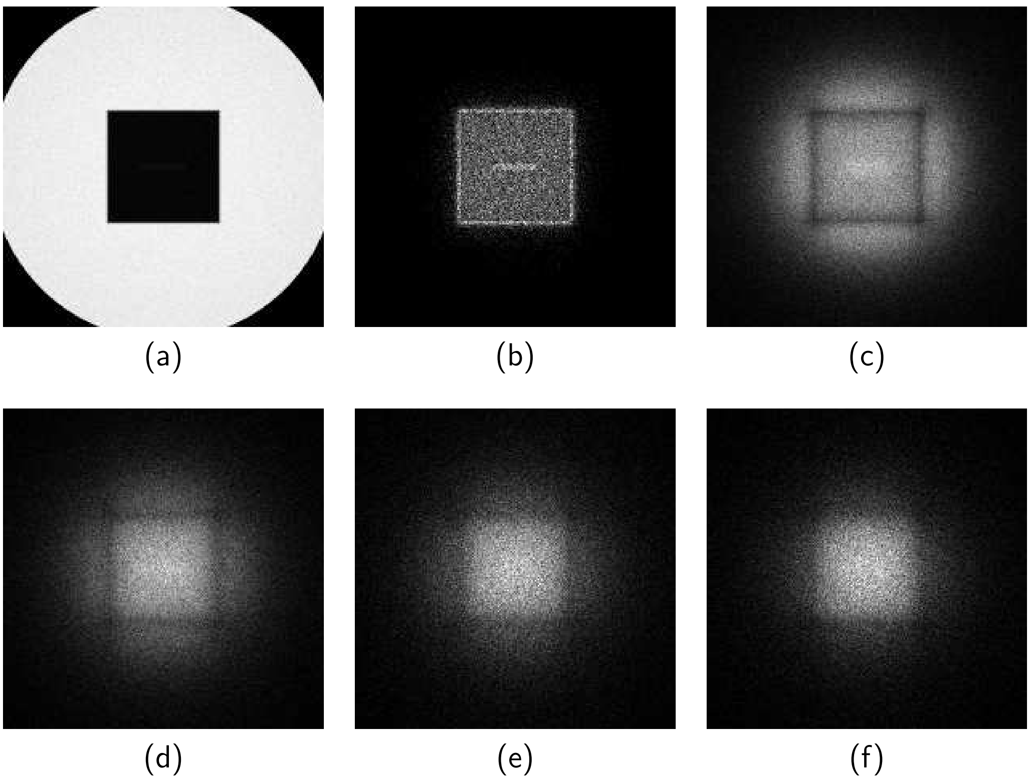

Figure A.1: Images given by simulation: (a) directly transmitted photons, (b) Rayleigh scattering, (c) Compton scattering, (d) multiple scattering order 2, (d) multiple scattering order 3, (e) multiple scattering order > 3.

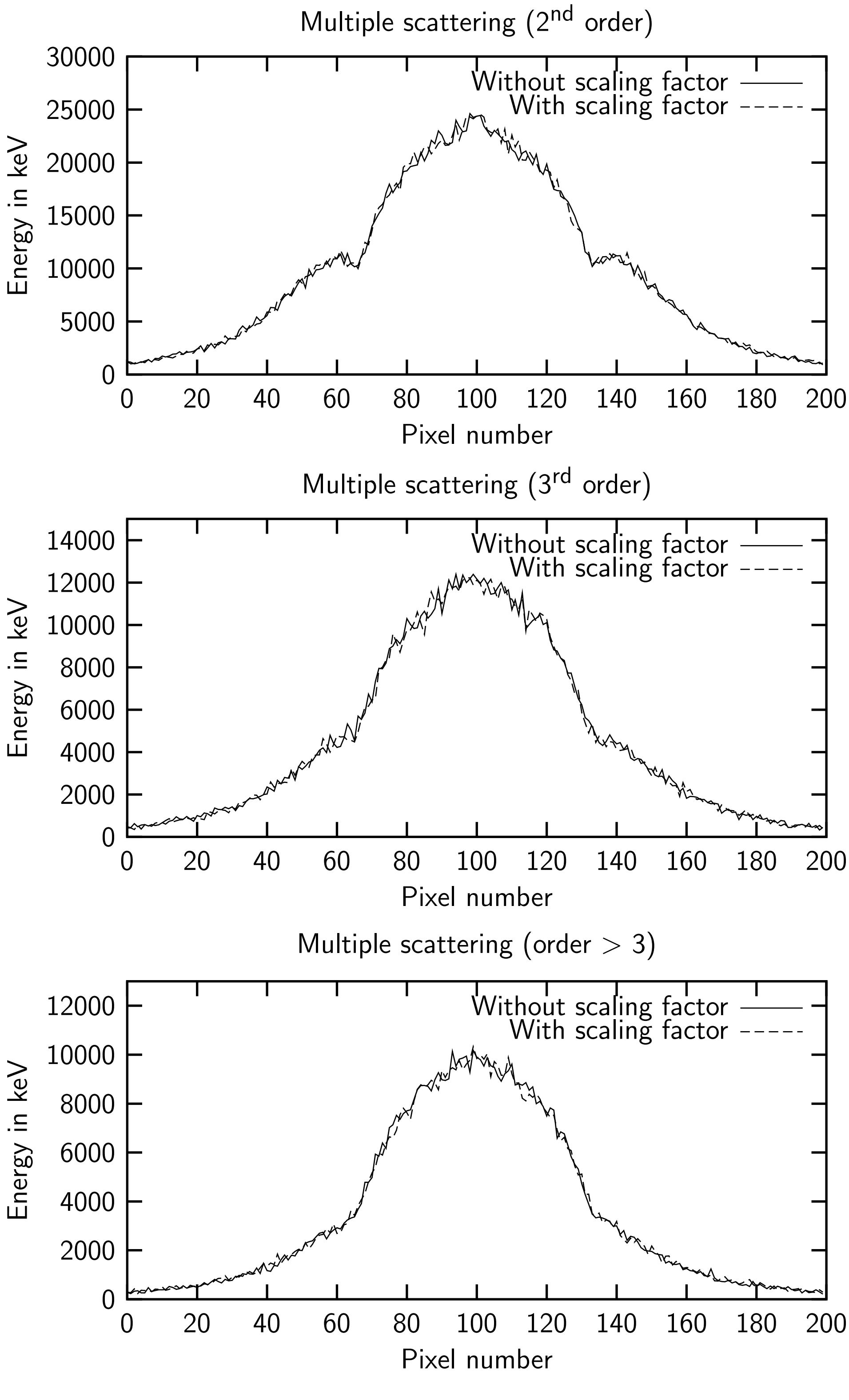

Figure A.2: Average vertical profiles of a simulation of a filter ($300 \times 300 \times 1$ *in mm) in lead at the front of an iron box of* $100 \times 100 \times 50$ *in mm, with a little cavity of* $20 \times 5 \times 2.5$ *in mm, using fan-beam of 400 keV.*

Appendix B

Flat field

In X-ray imaging, raw data have to be corrected before analysing. There is a difference in sensitivity between pixels [Ret98]. Flat field correction (Eq. B.1) allows to remove the effects of the non-uniform response of the CCD. It sets every pixel values in the same dynamic using:

$$I_{output}(x,y) = \frac{I_{input}(x,y) - I_{dark}(x,y)}{I_{ref}(x,y) - I_{dark}(x,y)} \tag{B.1}$$

with I_{output} the corrected image, I_{input} the measured image to correct, I_{dark} a measured image without incident beam and I_{ref} a measured image with full flow.

Fig. B.1 illustrates the effect of the flat field correction on a projection of a Gallium-Arsenide crystal plate acquired at ID19 beamline of ESRF.

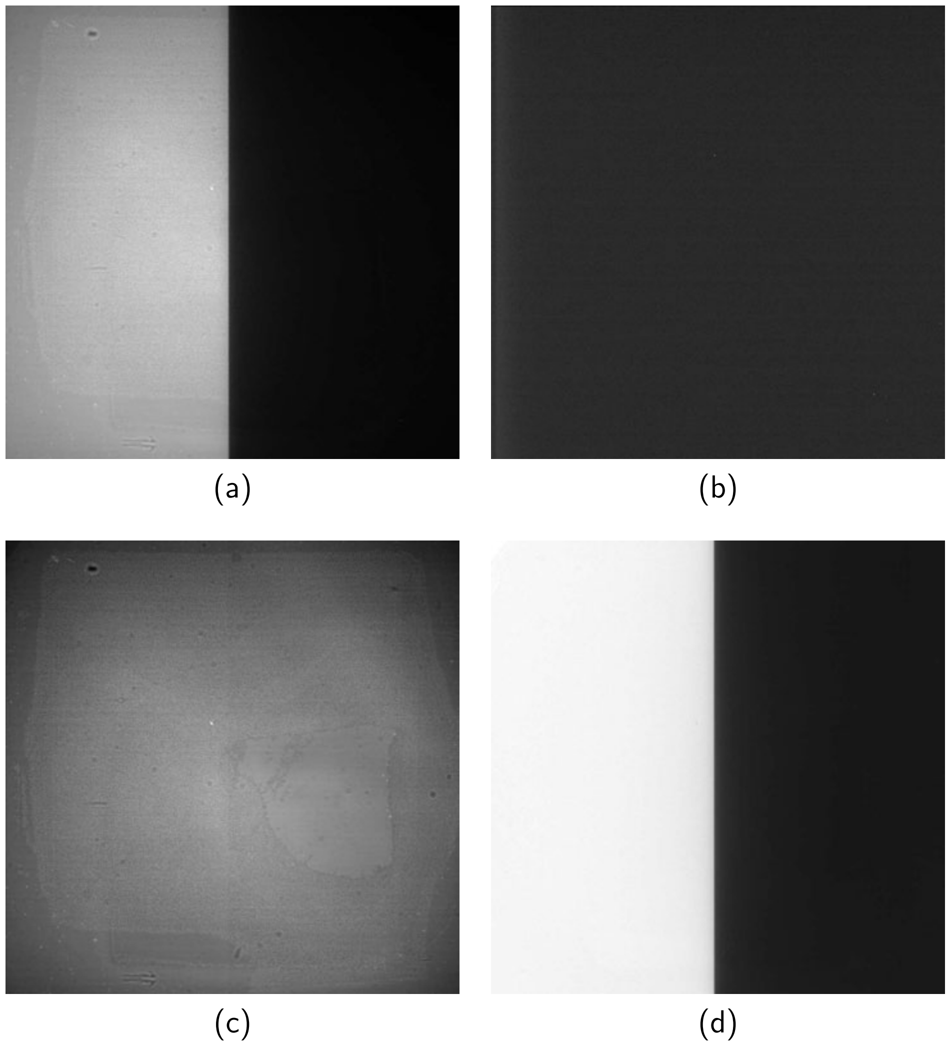

Figure B.1: Flat field correction. Pixel size: 1.9 μm. Synchrotron radiation: 33 keV in energy. (a) I_{input}, (b) I_{dark}, (c) I_{ref}, (d) I_{output}.

Appendix C

Parameters estimated by gnuplot

The following tables resume the parameters of the Eq. 2.12 estimated by gnuplot for the profiles corresponding to Fig. 2.19,

2^{nd} horizontal profile:

Final set of parameters	Asymptotic Standard Error	
a = 0.528695	+/- 0.0001602	(0.0303%)
b = -0.187731	+/- 0.0004134	(0.2202%)
c = 382.479	+/- 0.08206	(0.02146%)
d = 19.4464	+/- 0.1469	(0.7556%)
e = 1481.03	+/- 23.31	(1.574%)

1^{st} vertical profile:

Final set of parameters	Asymptotic Standard Error	
a = 0.527577	+/- 0.0001588	(0.03009%)
b = 0.179894	+/- 0.0004115	(0.2288%)
c = 467.752	+/- 0.07577	(0.0162%)
d = 13.7831	+/- 0.1261	(0.9147%)
e = 1144.1	+/- 16.53	(1.445%)

Error rates show that estimated parameters are very close to the data points set.

Appendix D

Deconvolution

D.1 Matlab programs

D.1.1 Iterative deconvolution function

The following program is the 1D deconvolution function:

```
function[out]=deconv1d(anInput, aKernel, aNumberOfIteration)
% Deconvolution 1D
%   anInput = observed data
%   aKernel = convolution kernel
%   aNumberOfIteration = number of iteration
%   out = corrected data after deconvolution
% Usage: tab_002_bis=deconv1d(tab_001_bis, kernel, 5);

% Initialize some sizes and vertor
[x, y] = size(anInput);
[xx, yy] = size(aKernel);
yy = y + yy - 1;

% For some optimsation
tmp = (yy - y) / 2;
tmp_plus_one = tmp + 1;

% Counter
i = 1;

% Accumulation buffer
out = anInput;

while i <= aNumberOfIteration
    % Convolution
```

```
    tab = conv(out, aKernel);

    % Difference with "iteration 0",
         % that is to say with observed data,
    % (note: the 'conv' function increase buffer size)
    err = anInput - tab(tmp_plus_one : y + tmp);

    % Accumulation
    out = out + err;

    i = i + 1;
end

% End of function
```

D.1.2 Test files

Function is used to generate a 1D signal

```
function[out]=CreateProfile(aRepeatSignalNumber,
                            aNumberOfEdge,
                            anEdgeSize)
% Create a signal 1D for testing
%   aRepeatSignalNumber = Repeat the signal
%                               aRepeatSignalNumber times
%   aNumberOfEdge = The number of edge of the profile
%   anEdgeSize = Size of an edge
% Usage: ideal_profile=CreateProfile(5, 4, 50)

% The total size of the profile
sub_signal_size = aNumberOfEdge * anEdgeSize;

% Create a vector and fill it with 0
out = zeros(1, sub_signal_size * aRepeatSignalNumber);

% Create an ideal profile
for i = 0 : aRepeatSignalNumber - 1
    out(anEdgeSize * 0 + i * sub_signal_size + 1 :
        anEdgeSize * 1 + i * sub_signal_size) = 1.0;

    out(anEdgeSize * 1 + i * sub_signal_size + 1 :
        anEdgeSize * 2 + i * sub_signal_size) = 0.5;

    out(anEdgeSize * 2 + i * sub_signal_size + 1 :
```

```
        anEdgeSize * 3 + i * sub_signal_size) = 0.0;

    out(anEdgeSize * 3 + i * sub_signal_size + 1 :
        anEdgeSize * 4 + i * sub_signal_size) = 0.5;
end

% End of function
```

Program used to test the 1D deconvolution function

```
% Needed for execution in octave, can be ignore using Matlab
clear;

% Defines
% The test signal is a step. The step can be repeated.

% Repeat the signal repeat_signal times
repeat_signal = 5;

% The number of edge of the profile
number_of_edge = 4;

% Size of an edge
edge_size = 50;

% The total size of the profile
sub_signal_size = number_of_edge * edge_size;

% Create the ideal profile (repeted 0 times)
tab = CreateProfile(repeat_signal, number_of_edge, edge_size);
[tab_width, tab_height] = size(tab);

% Load the detector response (convolution kernel)
load HOR_B_31;
kernel = HOR_B_31';
[kernel_width, kernel_height] = size(kernel);
half_of_kernel_height = (kernel_height - 1) / 2;

% Create a profile convolved by the detector response
% The conv function increase buffer size
tab_001 = conv(tab, kernel);
tab_001_bis = tab_001(half_of_kernel_height + 1 :
                      tab_height + half_of_kernel_height);
```

```
% 1st iteration
tab_002_bis = deconv1d(tab_001_bis, kernel, 1);

% 2nd iteration
tab_003_bis = deconv1d(tab_001_bis, kernel, 2);

% 24th iteration
tab_025_bis = deconv1d(tab_001_bis, kernel, 24);

% Select a ROI
offset_1 = sub_signal_size * repeat_signal / 2 - sub_signal_size / 2;
offset_2 = offset_1 + sub_signal_size + edge_size;

% Display result
plot(tab(offset_1 + 1 : offset_2))
hold on
plot(tab_001_bis(offset_1 + 1 : offset_2))
plot(tab_002_bis(offset_1 + 1 : offset_2))
plot(tab_003_bis(offset_1 + 1 : offset_2))
plot(tab_025_bis(offset_1 + 1 : offset_2))
hold off
```

D.2 Programmed iterative algorithm

Fig. D.1 presents the iterative algorithm. Arrows represent input/output files. Each box represents a program. *GetLogImage* is used to obtain sinogram from projections. *recons3d* reconstructs tomographic slices from sinogram. *SimuFromVoxel* simulates projections from a µmap (voxels). *Convolve1D* is used to convolve projections by impulse response of the detector. *Difference* gets difference pixel with pixel between two images. *Addition* gets addition pixel with pixel between two images.

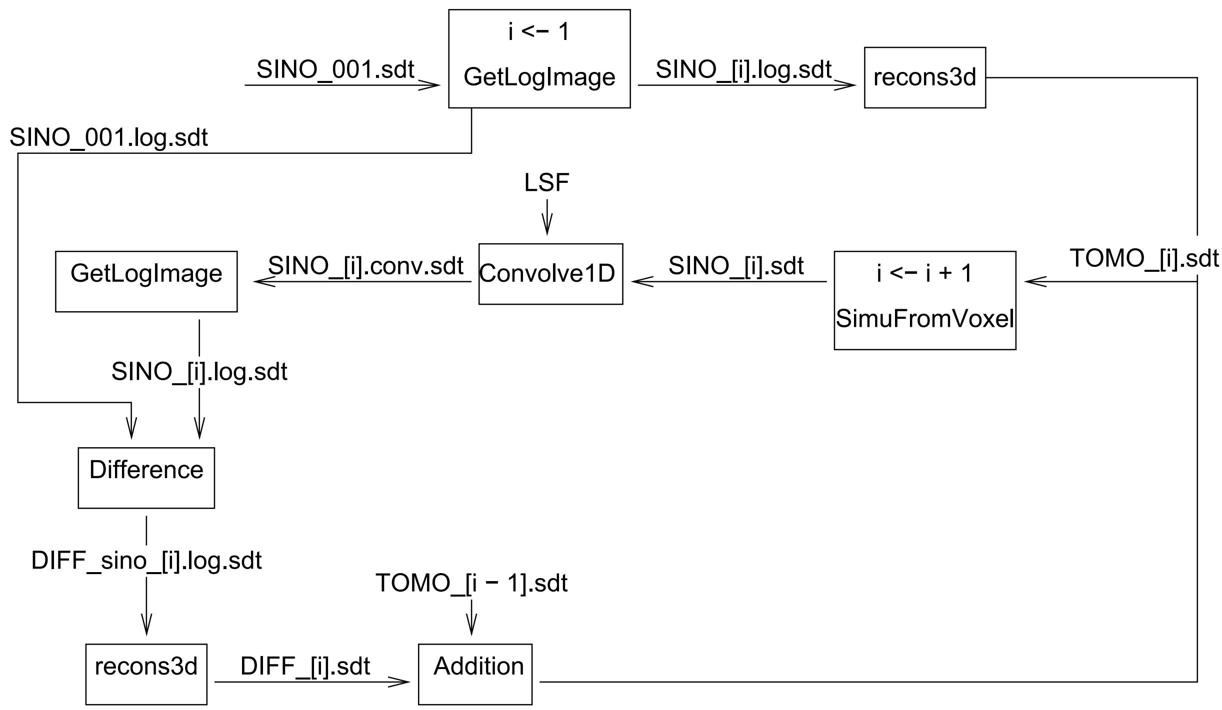

Figure D.1: Iterative deconvolution algorithm.